A model for the quasi-static and dynamic simulations of bevel gears

A. Pigé, Philippe Velex, R. Lanquetin, P. Cutuli

A model for the quasi-static and dynamic simulations of bevel gears

A. Pigé [a,b], P. Velex [b,*], R. Lanquetin [a], P. Cutuli [a]

[a] SAFRAN Helicopter Engines, R&T Department, 25 Avenue Joseph Szydlowski, Bordes 64510, France
[b] INSA Lyon, LaMCoS, UMR CNRS 5259, B^atiment Jean d'Alembert, 20 Avenue Albert Einstein, Villeurbanne CEDEX 69621, France

An original mesh interface model for the static and dynamic simulations of bevel gears is presented. It is based on the superposition of several elastic foundations and accounts for elastic couplings between points of contact, while no hypothesis on tooth contact locations is needed. Comparisons with experimental contact patterns and transmission errors prove that the mesh model is sound. The combination of a time-step integration scheme and a unilateral normal contact algorithm gives access to instant contact patterns, loads and transmission errors as opposed to the classic models based on quasi-static characteristics. It is shown that load is highly influential on contact conditions in bevel gears and that dynamic effects can induce overloads and oscillatory contact patterns in the vicinity of critical speeds, thus emphasizing the possible interactions between the local (contact) and global (system) scales.

1. Introduction

Bevel gears are widely used to transfer rotation between intersecting axes, particularly in large power density systems such as automotive transmissions, accessory and power gearboxes in airplanes and helicopters, etc., for which, reliability and noise control are critical and traditional standard such as ISO 10300 cannot be employed. In this context, the control of tooth contacts is crucial and efficient simulations of the instant contact patterns in the presence of errors and tolerances are needed. To date, the vast majority of the models in the literature deal with quasi-static calculations while the sparser dynamic models frequently use quasi-static characteristics such as mesh stiffness and transmission error as input data. With the exception of finite element models based on node-to-node or node-to-surface contact detections, the simulations of bevel gears rely on specific approaches to locate tooth contacts. Based on differential geometry, tooth contact analysis (TCA) makes it possible to generate tooth geometry, define machine tool settings and determine rigid-body kinematics [1,2]. By assuming continuous tangency between mating tooth flanks, contact points can be determined and the corresponding contact zones and pressure distributions be derived from the Hertzian theory. Several authors introduce a notion of surface of action, equivalent to that of base plane for spur and helical gears, so that its intersection with tooth flanks defines a curve along which contacts can potentially occur. Kolivand and Kahraman [3] employed this methodology together with ease-off surfaces, which represent the deviation of the actual tooth flanks from conjugate surfaces, and later extended their approach to account for measured tooth surfaces (Kolivand et al. [4]). Vivet et al. [5] directly used the penetrations calculated along the curve of potential

* Corresponding author.
E-mail address: Philippe.Velex@insa-lyon.fr (P. Velex).

Nomenclature

$\mathbf{C}$	damping matrix
C_{jmk}	elastic half-space coefficient of influence
d_i	rigid-body displacement of foundation node N_i
$\mathbf{F_q}$	vector of external forces on the gear pair
$\mathbf{F_w}$	gear-mesh excitation vector (for the whole gear pair)
$\mathbf{f_w}^{Cj}$	contribution of contact pair j to gear-mesh excitation vector
$\mathbf{F}(t,\mathbf{w},\mathbf{q})$	condensed force vector
$G(M), G_e$	shear coefficient of the Pasternak foundation (continuous and discrete form)
k_{ii}	stiffness of the ith foundation spring
$\mathbf{k_{qq}}, \mathbf{k_{qw}}, \mathbf{k_{wq}}$	stiffness matrices coupling a single elastic foundation to the gear body
$\mathbf{k_{ww}}$	stiffness matrix of an isolated elastic foundation
k_{Cj}	stiffness of the spring associated to contact pair j
$\mathbf{k_{ww}}^{Cj}$	contribution of contact pair j to the overall contact stiffness matrix
$\mathbf{K_{qq}}$	stiffness matrix of gear bodies and shafts
$\mathbf{K_{qw}}$	stiffness matrix coupling gear bodies and teeth
$\mathbf{K_{ww}}$	stiffness matrix of all tooth pairs in mesh
$\mathbf{K}(t,\mathbf{w},\mathbf{q})$	condensed stiffness matrix of the gear pair
$\mathbf{M}$	mass matrix of the gear pair
M_{mj}	point of the tooth flank ($m=1$ refers to the pinion, $m=2$ to the gear)
N_i	node n°i of a tooth (i.e. elastic foundation)
$\mathbf{n}$	outward unit normal to the tooth flank
O_m	centre of the gear body ($m=1$ refers to the pinion, $m=2$ to the gear)
$\mathbf{q}$	degrees of freedom of the gear pair
$\mathbf{S}(N_i)$	structural vector
U_{Cj}	strain energy stored in the contact stiffness element j
$U_{shear}, U_{springs}$	strain energies stored in a single elastic foundation
$\mathbf{w}$	vector of teeth deflections
δe_j	initial separation of potential contact pair j
δ_{mj}	contact deflection of cell j ($m=1$ refers to the pinion, $m=2$ to the gear)
φ_i	shape function of bidimensional finite elements

contact, thus eliminating the need for a precomputed ease-off surface and later adapted the derivation of surfaces of action for misaligned gears [6]. Due to the complex geometry of spiral bevel gears, three-dimensional FEM models seem appropriate for quasi-static analyzes under load. In 2002, Argyris et al. [2] proposed a software code integrating the synthesis, the determination of machine-tool settings, the kinematic analysis and a quasi-static simulation of hypoid gears. Tooth flanks were discretized using specific finite elements to reproduce analytical geometries with relatively coarse meshes. Hotait et al. [7] investigated the effect of misalignments on the root stresses in hypoid gears and found a good agreement between their finite element results and the measurements from strain gauges cemented at tooth roots. A finite-element model was also used by Ding et al. [8] within an optimization framework. Vijayakar [9] solved the contact problem by a semi-analytical method allowing the use of coarser finite elements while keeping refined contact discretisation. The structural compliance associated with tooth bending and shear, gear body elasticity, etc. is often characterised by using coefficients of influence, generally derived from finite element models of a few adjacent teeth [3,10–13]. Gosselin et al. [10] combined this approach with a Hertzian contact model, whereas Simon [11,12] sliced the curves of potential contacts into a number of contacting thin cylinders of variable radii. In the context of conformal contacts, De Vaujany et al. [13] used the solution of Boussinesq for elastic half spaces. Alternative methods can be employed to estimate the influence coefficients associated with structural tooth deflections. Vaidyanathan et al. [14], Kolivand and Kahraman [3] used a Rayleigh-Ritz method applied to sectors of annular plates for straight bevel gears and to a shell model for spiral-bevel/hypoid gears. Gosselin et al. [15] introduced a finite strip method, Wagner et al. [16] implemented a boundary element method while, using Tredgold's approximation (Dooner et al. [17]), Vivet et al. [5] sliced teeth into equivalent thin spur gear teeth assimilated to clamped-free beams, and assumed cylinder-to-cylinder contacts between the slices.

Beyond these quasi-static analyzes cited above, most of the published work on gear dynamics relies on global lumped parameter models for which, the contact conditions between the teeth are independent of speed. The mesh stiffness functions and transmission errors are therefore derived from quasi-static simulations. To the authors' best knowledge, this approach was first applied to spiral bevel gears in 1977 by Astridge and Salzer [18], who also accounted for shaft bending, bearings and housings. Cheng and Lim [19] solved the dynamic problem in the frequency domain using tooth flank surfaces derived from simulations of the machining process and the contact conditions at a given roll angle. Later, the authors enhanced this model by considering time-varying mesh stiffness functions and transmission errors [20]. Sainte-Marie [21] provided a review of more recent dynamic models and proposed a global

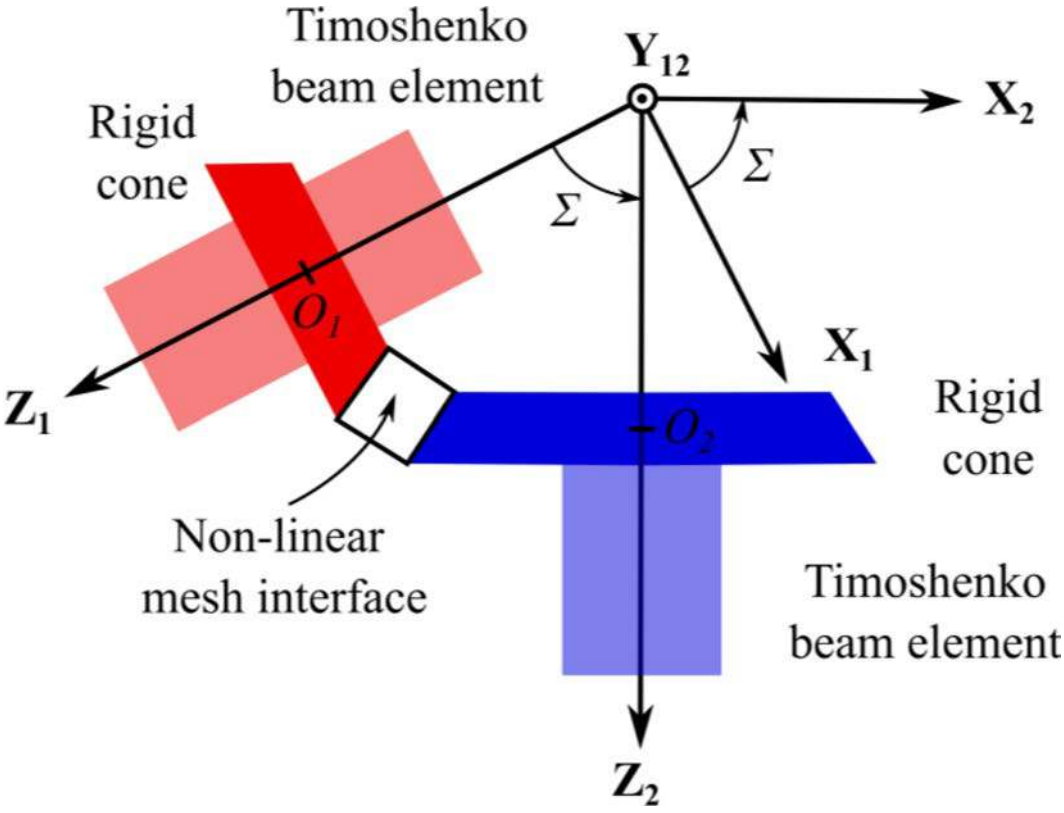

Fig. 1. Schematic representation of the model, coordinate system of reference.

model adapted to multi-mesh transmissions. More recently, Yang et al. [22] designed spiral bevel gears with parabolic or higher-order no-load transmission errors and analyzed the influence of the corresponding micro-geometries on dynamic excitations. Using Timoshenko beam elements for shafts and gears, Yavuz et al. [23] solved the corresponding state equations in the frequency domain. In an effort to include the influence of the mechanical environment, substructures were used to simulate housings by Yang et al. [24], while Wang et al. [25] modelled bearings as varying lumped stiffness matrices. In contrast with most global models where tooth mesh elasticity is assimilated to one unique stiffness element, Wang et al. [26] extended the model originally developed by Peng [27] and considered one mesh point per tooth pair, allowing the dynamic mesh force on each tooth to be extracted. Finally, the dynamic contact conditions in bevel gears have been introduced by Wagner et al. [16] Thoret-Bauchet [28] via influence coefficients in a multi-body dynamic software code and a specific dynamic model of spiral bevel gears, respectively.

The present paper is aimed at presenting an efficient modelling strategy for straight and spiral bevel gears, valid in quasi-static and dynamic conditions. An original mesh interface based on elastic foundations [29] is proposed. Contrary to the vast majority of the dynamic models in the literature, quasi-static transmission errors and/or time-varying mesh stiffness functions are not considered as *a-priori* known excitations. No hypotheses on the locations of the contacts are introduced and the equations of motion along with the instant contact conditions on tooth flanks are simultaneously solved. The proposed methodology makes it possible to track contacts with precision and use refined elastic models, while keeping calculation times far below those associated with nonlinear FEM solutions. The theoretical background is presented in Section 1, which includes rigid-body kinematics, tooth structural (linear) deflections, and instant contact stiffness along with the solution technique for the equations of motion and the contact problem. The proposed methodology is then applied to the quasi-static simulations of an actual gear with assembly errors, using measured tooth flank topographies. The calculated quasi-static transmission errors and tooth contact patterns are compared with experimental measurements. Finally, a number of simulation results are presented, which highlight the potential of the proposed methodology and the interest of simultaneously dealing with the equations of motion and the contact conditions on tooth flanks, particularly in the vicinity of critical speeds.

2. Dynamic model

2.1. Generalities

The generic bevel gear model used in this paper is schematically represented in Fig. 1. The shafts, inclined at an angleΣ to each other, are discretised into 2-node Timoshenko beam elements with 6 degrees-of-freedom per node to account for bending, torsion and

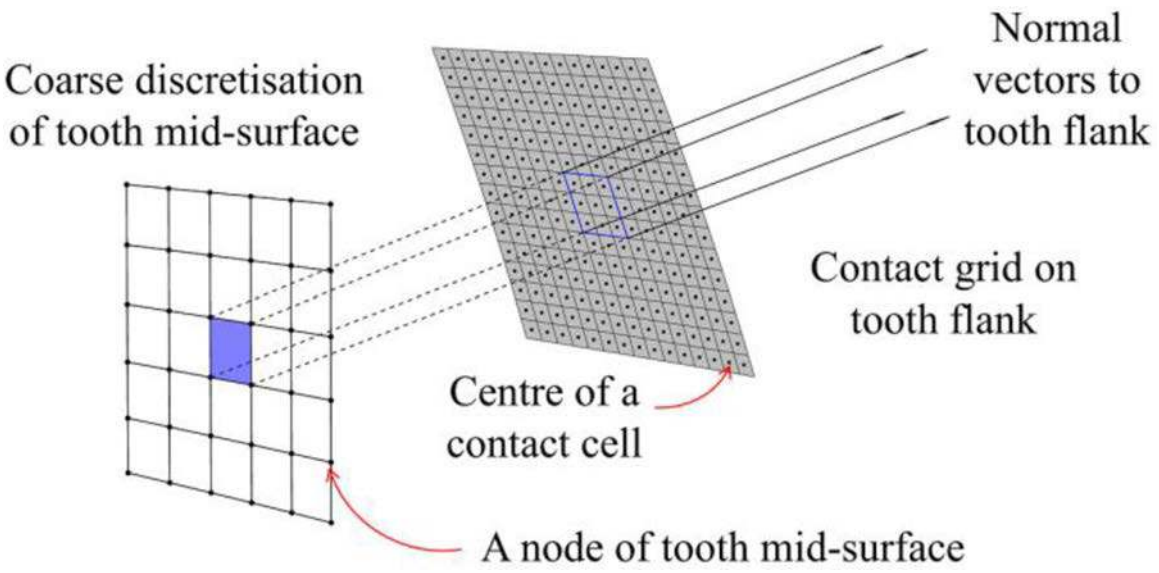

Fig. 2. Discretisation of tooth flank and tooth mid-surface (9 contact cells are connected to the structural element in this example).

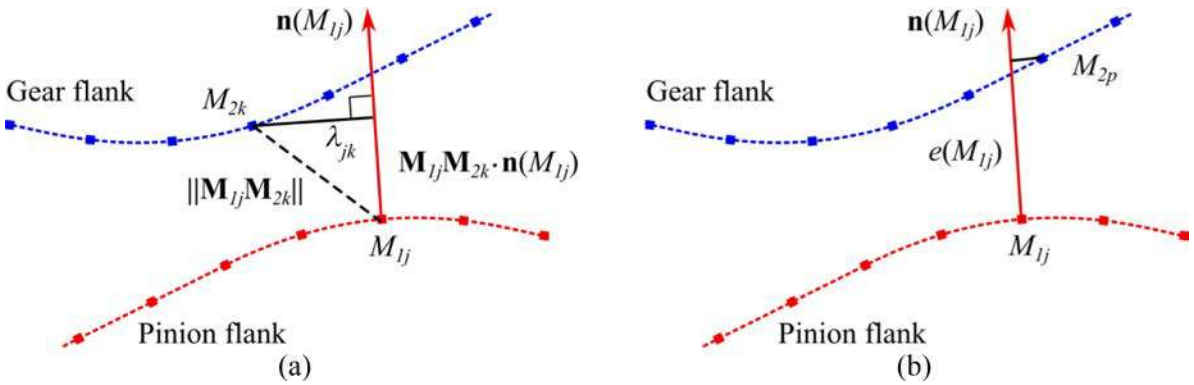

Fig. 3. (a) distances between a point of the pinion and a random point of the gear, (b) separation distance of a potential contact pair.

traction. The pinion and gear bodies are assimilated to two rigid cones with 6 degrees-of-freedom expressed at their respective centres O_1 and O_2. The bearings and couplings are simulated by lumped stiffness elements, which can be inserted at any node in the model.

The pinion and gear teeth are connected via a specific time-varying non-linear mesh interface. Tooth structural effects are global and induce long range elastic couplings (over the entire tooth surface for example) as opposed to contact deflections, which are more localised and characterised by steeper gradients. Using measured flank topographies as input data, the proposed mesh-interface aims at estimating pressure distributions accurately, including the case of contact ellipses close to line contacts. The basic principle consists in employing a two-scale discretisation comprising: (a) coarse meshes attached to tooth mid-surfaces to account for tooth structural effects, and (b) refined grids in order to determine contact features (contact areas, pressures) with precision. The two discretisation levels are interdependent since several contact cells of the fine grid are associated with every element of the mid-surface (coarser grid) as illustrated in Fig. 2 (nine contact cells for one structural element in this example). Degrees of freedom are attributed to the nodes of the coarse grids only, which are used to interpolate the structural deflections. The contact deflections on the refined grids are approximated by using a semi-analytical method to reduce the computational times for deflections while the large point density makes it possible to use well-established point-to-point contact detection techniques.

2.2. Reference state-rigid-body geometry and kinematics

Actual tooth flank geometries are defined externally based on point coordinates derived from metrological controls. Following [3], tooth mid-surfaces are assimilated to portions of cylinders which are used as the physical supports of the coarser discretisation grids. The active tooth flank geometries are approximated by polynomial functions and are re-discretised in order to generate the finer grids [28]. Possible manufacturing deviations can be directly incorporated by modifying the location of the centre of each contact cell of this

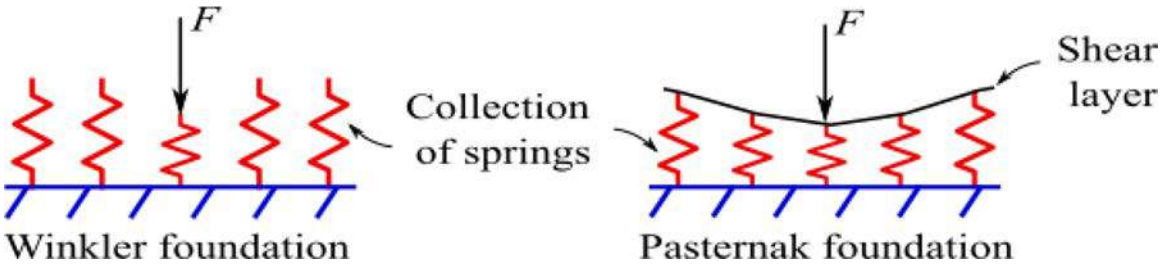

Fig. 4. Winkler and Pasternak foundations submitted to a lumped force.

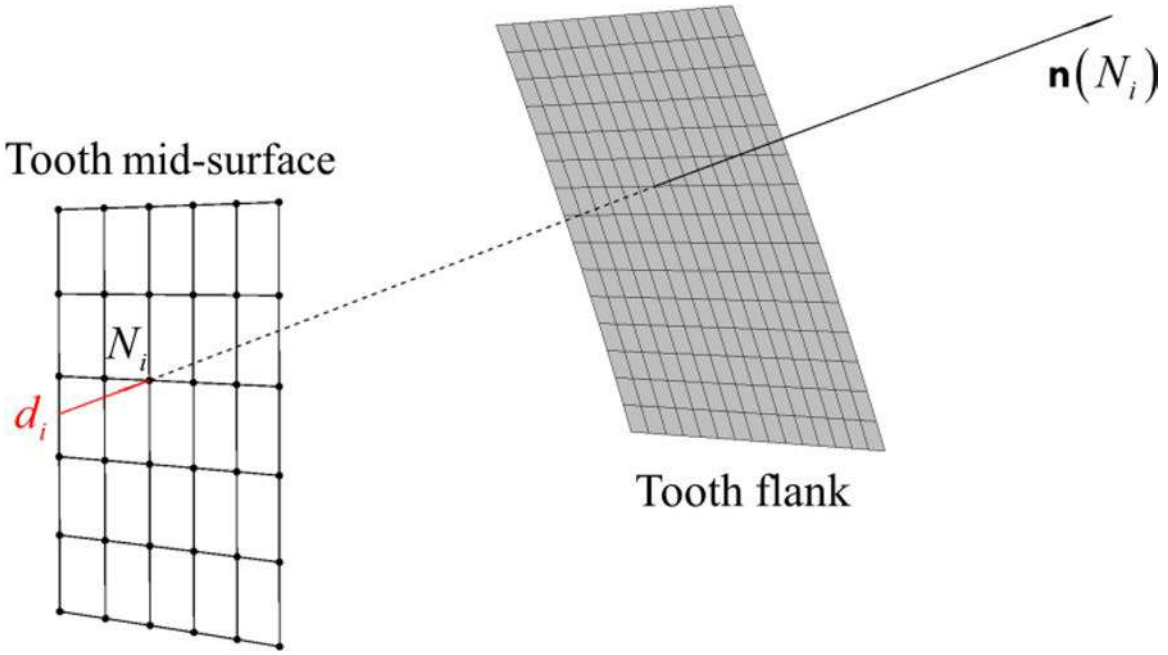

Fig. 5. Projection of rigid body displacements at a node of tooth mid-surface.

finer grid.

The reference state is derived from the actual positions of the contact cell centres (refined grid), which are denoted by M_{mj}, where m refers to the pinion (1) or to the gear (2). Conventionally, all the tooth surface point coordinates and outward unit normal vectors are expressed in the coordinate system $(\mathbf{X_2}, \mathbf{Y_2}, \mathbf{Z_2})$ attached to the driven member (Fig. 1) and the teeth on the pinion and gear are matched. Focusing on one tooth pair, potential contact points are sought by considering every point M_{1j} on the pinion flank and calculating its distances λ_{jk} to the 5 nearest points on the corresponding gear tooth surface as (Fig. 3(a)):

$$\lambda_{jk}^2 = \| \mathbf{M}_{1j}\mathbf{M}_{2k} \|^2 - \left(\mathbf{M}_{1j}\mathbf{M}_{2k} \cdot \mathbf{n}(M_{1j})\right)^2 \tag{1}$$

where $\mathbf{n}(M_{1j})$ refers to the outward unit normal vector with respect to the pinion flank.

Point M_{2p}, minimising this distance, lies approximately on the normal at point M_{1j} (Fig. 3(b)) so that their initial normal separation is:

$$e(M_{1j}) \simeq \mathbf{M}_{1j}\mathbf{M}_{2p} \cdot \mathbf{n}(M_{1j}) \tag{2}$$

Contacts in rigid-body conditions occur where the initial separation between all the mating tooth pairs is minimal. Therefore, separations in rigid-body conditions read:

$$\delta e_j = e(M_{1j}) - \min_\ell [e(M_{1\ell})] \tag{3}$$

where the minimum $\min_\ell [e(M_{1\ell})]$ is sought over all the potential contact points on several tooth pairs potentially in mesh.

The procedure is repeated at every time-step with updated angular positions based on rigid-body kinematics. In order to limit the number of calculations but be able to capture possible interferences and corner contacts, N_t tooth pairs in the vicinity of the contacting

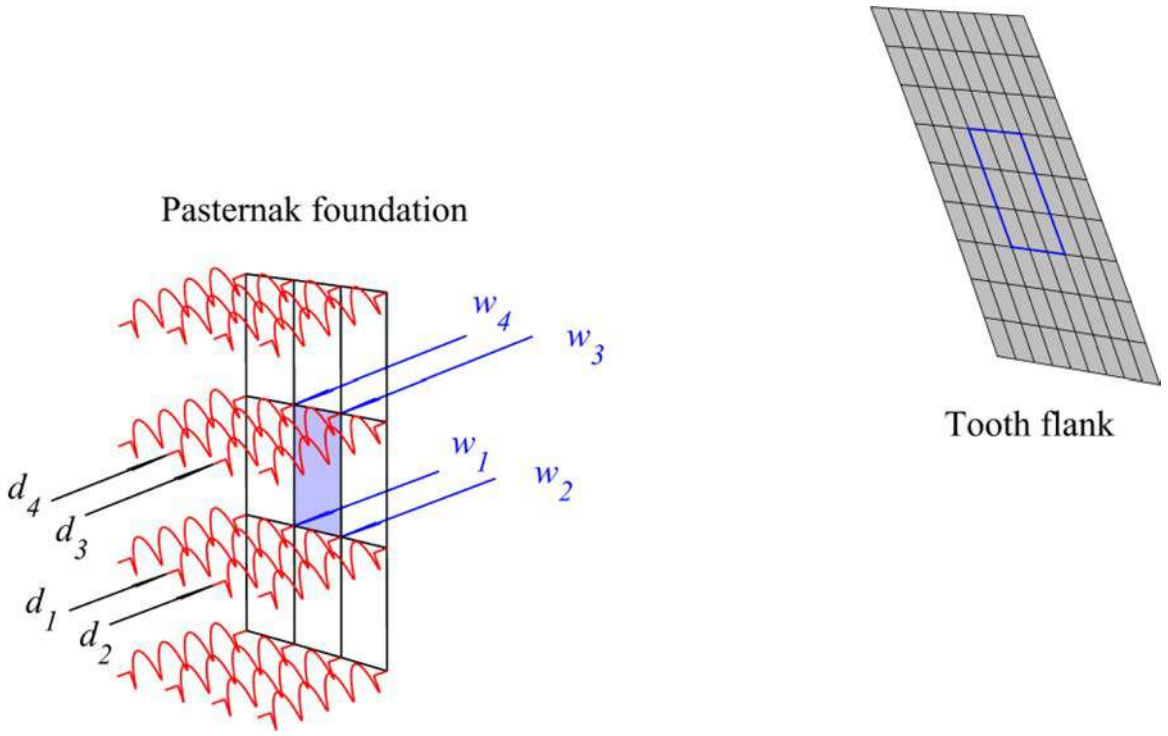

Fig. 6. Coupling of Pasternak foundations and gear bodies by stiffness elements.

pair(s) in rigid-body conditions are inspected, such that:

$$N_t = \lfloor \varepsilon_t \rfloor + 2 \tag{4}$$

where $\lfloor \varepsilon_t \rfloor$ is the integral part of the total contact ratio ε_t defined by ISO 10300.

2.3. Tooth structural deflections and coarser grids

The classic simulations in gear dynamics often rely on thin-slice models also known as Winkler foundations, i.e. collections of independent stiffness elements (springs), which cannot account for elastic couplings between neighbouring contact points. Following Seager [30], Schmidt et al. [31], Ajmi and Velex [32], these limitations can be overcome by Pasternak foundations [29] which connect the springs via a shear layer (Fig. 4). For cylindrical gears, their benefit compared to the classic Winkler model has been highlighted in the case of edge or partial contacts [32].

In what follows, the shear layers (one per tooth) are situated at tooth mid-surfaces and are discretised into quadrangular finite elements (coarse grid) with four nodes N_i at their corners. Each node has a single degree of freedom (DOF) denoted w_i. These DOFs represent deflections at tooth mid-surface along a straight line passing by N_i and normal to the tooth flank. A direct stiffness element k_{ii} is connected to each node.

The connection between the Pasternak foundations and rigid gear bodies is schematically illustrated in Figs. 5 and 6. Each foundation spring is connected to the corresponding tooth mid-surface at one extremity, while a displacement d_i depending on gear body displacements is applied at its other extremity. Using the moment transfer formula for infinitesimal rigid-solid displacement screws, d_i can be expressed in terms of the degrees-of-freedom $\mathbf{q}(O_m)$ at the cone centre as:

$$d_i = \mathbf{S}(N_i)^T \mathbf{q}(O_m) \tag{5}$$

with $\mathbf{S}(N_i)^{\mathrm{T}} = \left(\mathbf{n}(N_i)^{\mathrm{T}}, \quad (\mathbf{n}(N_i) \times \mathbf{N_i O_m})^{\mathrm{T}} \right)$

$\mathbf{n}(N_i)$, the unit outward normal vector to the tooth flank at the orthogonal projection of node N_i on flank surface.

Each foundation spring deflection being $d_i + w_i$, the resulting strain energy reads:

$$U_{\text{springs}} = \frac{1}{2} \sum_i k_{ii} \left(w_i + \mathbf{S}(N_i)^T \mathbf{q}(O_m) \right)^2 \tag{6}$$

and, imposing no shear stress at the edges of the elastic foundation, the strain energy of the shear layer is expressed as (continuous form):

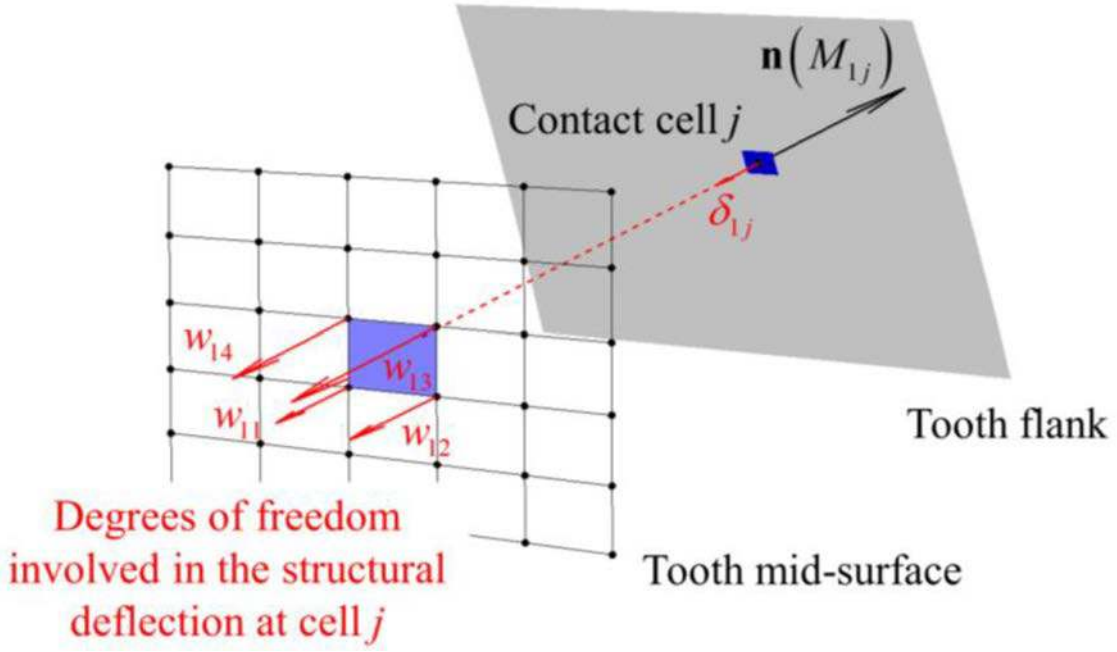

Fig. 7. Combination of structural and contact deflections.

$$U_{\text{shear}} = \frac{1}{2}\int_D \mathrm{G}(M)(\mathbf{grad}w(M))^2 dS \tag{7}$$

where $\mathrm{G}(M)$ is the local shear coefficient (to be determined) at the centre of the elemental surface of area dS.

The displacements fields are discretised as $\mathrm{w}(M) = \sum_{i=1}^{4} \varphi_i(M)\, w_i$, where φ_i are linear elemental shape functions (Lagrange polynomial functions), so that:

$$U_{\text{shear}} = \frac{1}{2}\sum_i \sum_j w_i \int_D \mathrm{G}(M)\mathbf{grad}\varphi_i(M) \cdot \mathbf{grad}\varphi_j(M)\, dS\, w_j \tag{8}$$

Using Lagrange's equations, the following stiffness matrices can be identified:

$$\begin{cases} \dfrac{\partial\left(U_{springs} + U_{shear}\right)}{\partial \mathbf{w}} = \mathbf{k_{ww}}\,\mathbf{w} + \mathbf{k_{wq}}\,\mathbf{q}(O_m) \\ \dfrac{\partial\left(U_{springs} + U_{shear}\right)}{\partial(\mathbf{q}(O_m))} = \mathbf{k_{qw}}\,\mathbf{w} + \mathbf{k_{qq}}\,\mathbf{q}(O_m) \end{cases} \tag{9}$$

where matrix $\mathbf{k_{ww}}$ represents the contribution of an isolated foundation and reads:

$$\mathbf{k_{ww}}(i,j) = k_{ii}\delta_{ij} + \int_D \mathrm{G}(M)\mathbf{grad}\varphi_i \cdot \mathbf{grad}\varphi_j\, dS \tag{10}$$

with $\delta_{ij} = 1$ if $i = j$ and $\delta_{ij} = 0$ if $i \neq j$.

Based on classic finite element methodologies, the integrals are computed by transfer to a reference element and assembly of the contributions of all the elements. To simplify the integration and identification of the foundation parameters, $\mathrm{G}(M)$ is assumed uniform over each structural surface element.

The following matrices represent the connection between the teeth and gear bodies:

$$\mathbf{k_{wq}} = \mathbf{k_{qw}^T} \quad \text{with} \quad \mathbf{k_{qw}} = [\,k_{11}\,\mathbf{S}(N_1) \quad \ldots \quad k_{nn}\,\mathbf{S}(N_n)\,] \tag{11}$$

$$\mathbf{k_{qq}} = \sum_i k_{ii}\mathbf{S}(N_i)\mathbf{S}(N_i)^T \tag{12}$$

In view of the actual tooth geometry, no analytical solution can be found, which would lead to closed-form expressions for the elastic parameters of the foundation. The stiffness k_{ii} and the shear parameters G are therefore identified based on the minimisation of the difference between the displacements given by a solution of reference (a 3D finite element, a plate [14] or shell model of the teeth [3] for instance) and those derived from the foundation (annex 1).

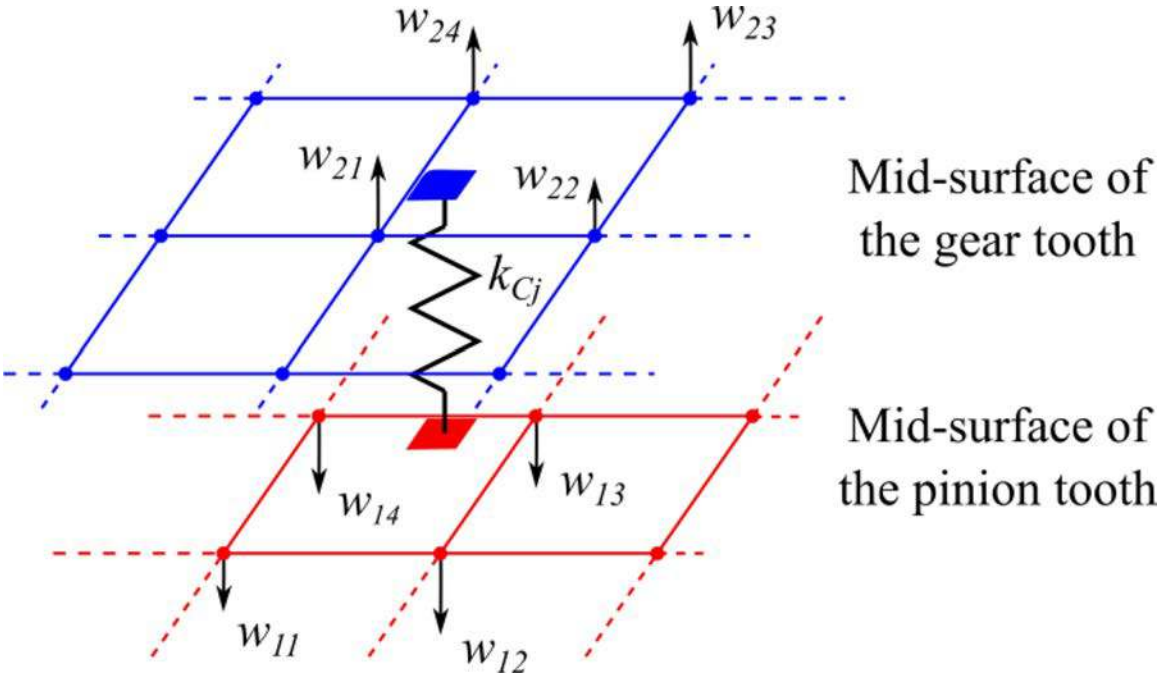

Fig. 8. Contact stiffness element J and parameters involved in the derivation of strain energy.

2.4. Contact deflections

A Winkler model is inserted between the two Pasternak foundations (one for a pinion and a gear tooth in mesh) in order to account for contact elasticity. Its stiffness elements are determined from the elastic half-space theory assuming that contact deflections are nil at tooth mid-surfaces [33,34] (Fig. 7). The Winkler foundation approach for the finer grid is justified by the smaller range of contact elastic couplings compared with those induced by structural deflections [32] and the fact that it leads to a simple and effective contact algorithm in static and dynamic conditions [35].

However, further corrections are introduced to account, even approximately, for contact convectivity. The contact deflection at cell j can be determined from the forces acting on all the cells$f_k$as:

$$\delta_{1j} + \delta_{2j} = \sum_k (C_{1kj} + C_{2kj}) f_k \tag{13}$$

with C_{1kj}, C_{2kj}, the elastic half-space coefficients of influence between cells j and k on the pinion (index 1) and gear (index 2), which are determined in a single run before the simulation (annex B). The contact stiffness of the Winkler foundation is defined as:

$$k_{Cj} = \frac{f_j}{\delta_{1j} + \delta_{2j}} = \frac{f_j}{\sum_k (C_{1kj} + C_{2kj}) f_k} \tag{14}$$

which, supposing a uniform force distribution ($f_j = f_k$) over the contact zone, leads to:

$$k_{Cj} \approx \frac{1}{\sum_k (C_{1kj} + C_{2kj})} \tag{15}$$

$\sum_k (C_{1kj} + C_{2kj})$is truncated to the neighbouring cells, which contribute most to the deflection at cell j, keeping in mind that contact convectivity is spatially more limited than the structural one.

The structural deflections of a pinion tooth are evaluated at P_{1j}, points at tooth mid-surfaces such that lines $(P_{1j}M_{1j})$ are normal to tooth flanks. Points P_{2j} are defined similarly on the gear. Points M_{1j} and M_{2j} come into contact when their total deflection, including contact flattening δ_{1j} and δ_{2j}, equates their initial separation in rigid-body conditions, hence:

$$-\left[\mathrm{w}(P_{1j}) + \delta_{1j} + \mathrm{w}(P_{2j}) + \delta_{2j}\right] = \delta e_j \tag{16}$$

Approximating the structural displacements at P_{1j} and P_{2j} in (16) using the shape functions of the foundation structural elements (coarse grid) yields the following contact compression:

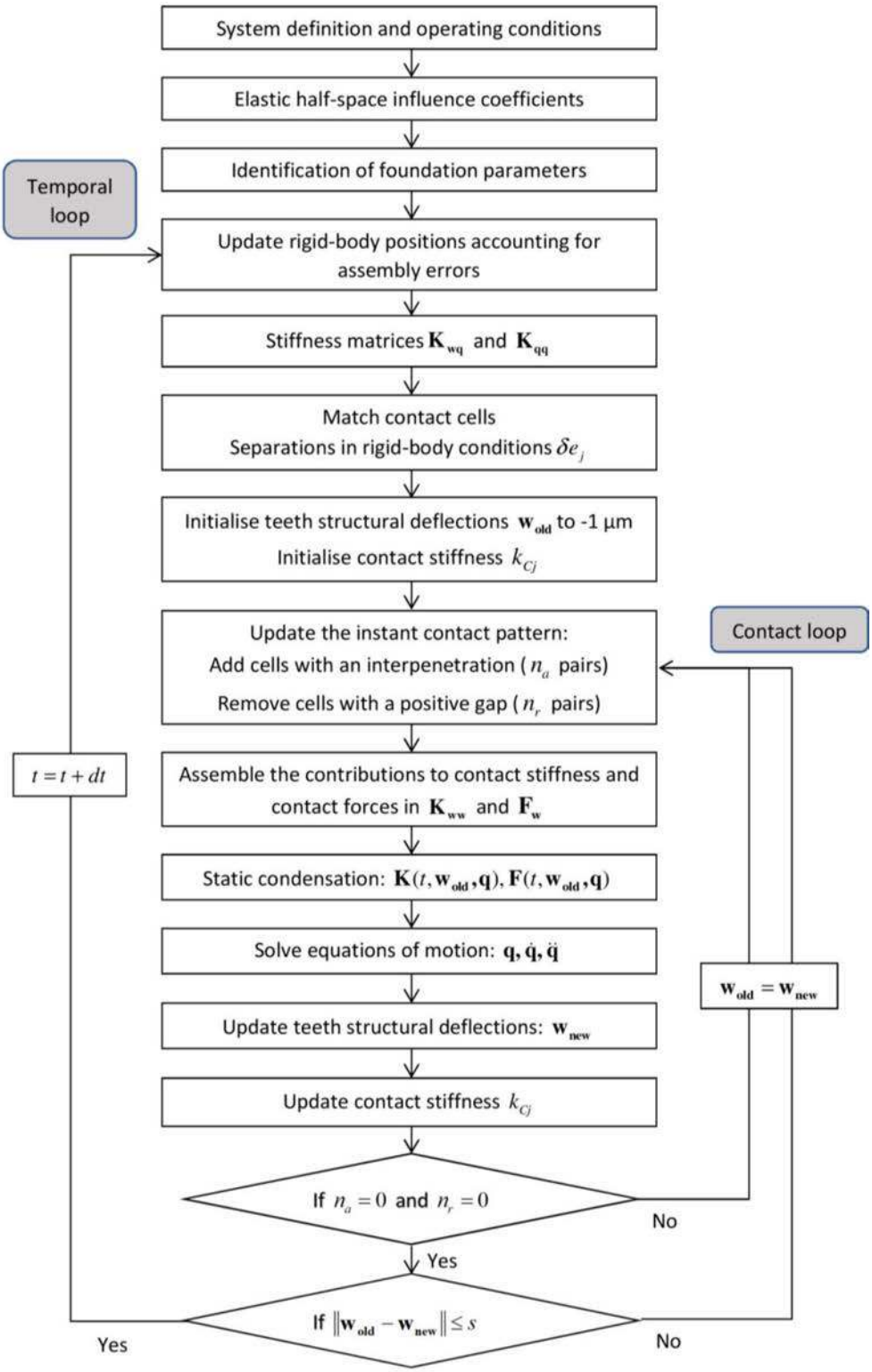

Fig. 9. Flowchart of the solution procedure.

$$\delta_{1j} + \delta_{2j} = -\delta e_j - \boldsymbol{\varphi}_{12j}^T \mathbf{w}_{12j} \tag{17}$$

Table 1
Gear data.

Blank data	Pinion	Gear
Number of teeth	37	44
Transverse module (at heel, on the pitch cone)	1,55 mm	
Mean cone distance	50 mm	
Pressure angle	20°	
Face width	7 mm	
Tooth height (heel)	3,43 mm	
Inner spiral angle	−2°44′	
Outer spiral angle	2°33′	
Hand of spiral	RH	LH
Young's modulus	200 GPa	
Poisson's ratio	0,3	
Accuracy class (ISO 17,485:2006(F))	5	

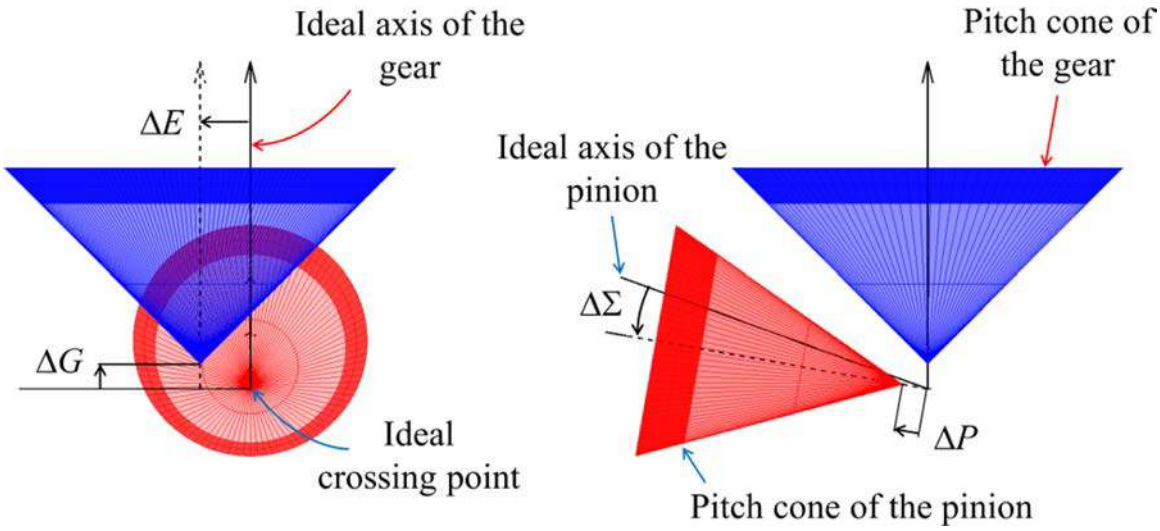

Fig. 10. Assembly errors under consideration.

Table 2
Assembly error amplitudes.

Configuration	ΔE [mm]	ΔP [mm]	ΔG [mm]	$\Delta\Sigma$ [°]
1	−0,24	0,17	−0,01	0,02
2	0,01	0,05	0,01	0,10

where:

$$\mathbf{w}_{12j} = \langle w_{11}, \ldots, w_{14}, w_{21}, \ldots, w_{24} \rangle^T$$

which comprises all the degrees of freedom of the pinion and gear tooth surfaces involved in the structural deflection at points P1j and P2j

$\boldsymbol{\varphi}_{12j}^T = \langle\, \varphi_1(P_{1j}) \quad \cdots \quad \varphi_4(P_{1j}) \quad \varphi_1(P_{2j}) \quad \cdots \quad \varphi_4(P_{2j}) \,\rangle$ are all the relevant (linear) shape functions associated with the surface finite elements on the pinion and gear teeth which are connected by the stiffness element j

If the right-hand side of (17) is positive, the pair is included in the contact pattern and the strain energy stored in the corresponding stiffness element (Fig. 8) is:

$$U_{Cj} = \frac{1}{2} k_{Cj} \left(\delta_{1j} + \delta_{2j} \right)^2 \tag{18}$$

Injecting (17) into (18) relates this strain energy to structural deflections and initial normal deviations in rigid-body conditions:

$$U_{Cj} = \frac{1}{2} \mathbf{w}_{12j}^T \left(k_{Cj} \boldsymbol{\varphi}_{12j} \boldsymbol{\varphi}_{12j}^T \right) \mathbf{w}_{12j} + \mathbf{w}_{12j}^T k_{Cj} \delta e_j \boldsymbol{\varphi}_{12j} + \frac{1}{2} k_{Cj} \delta e_j^2 \tag{19}$$

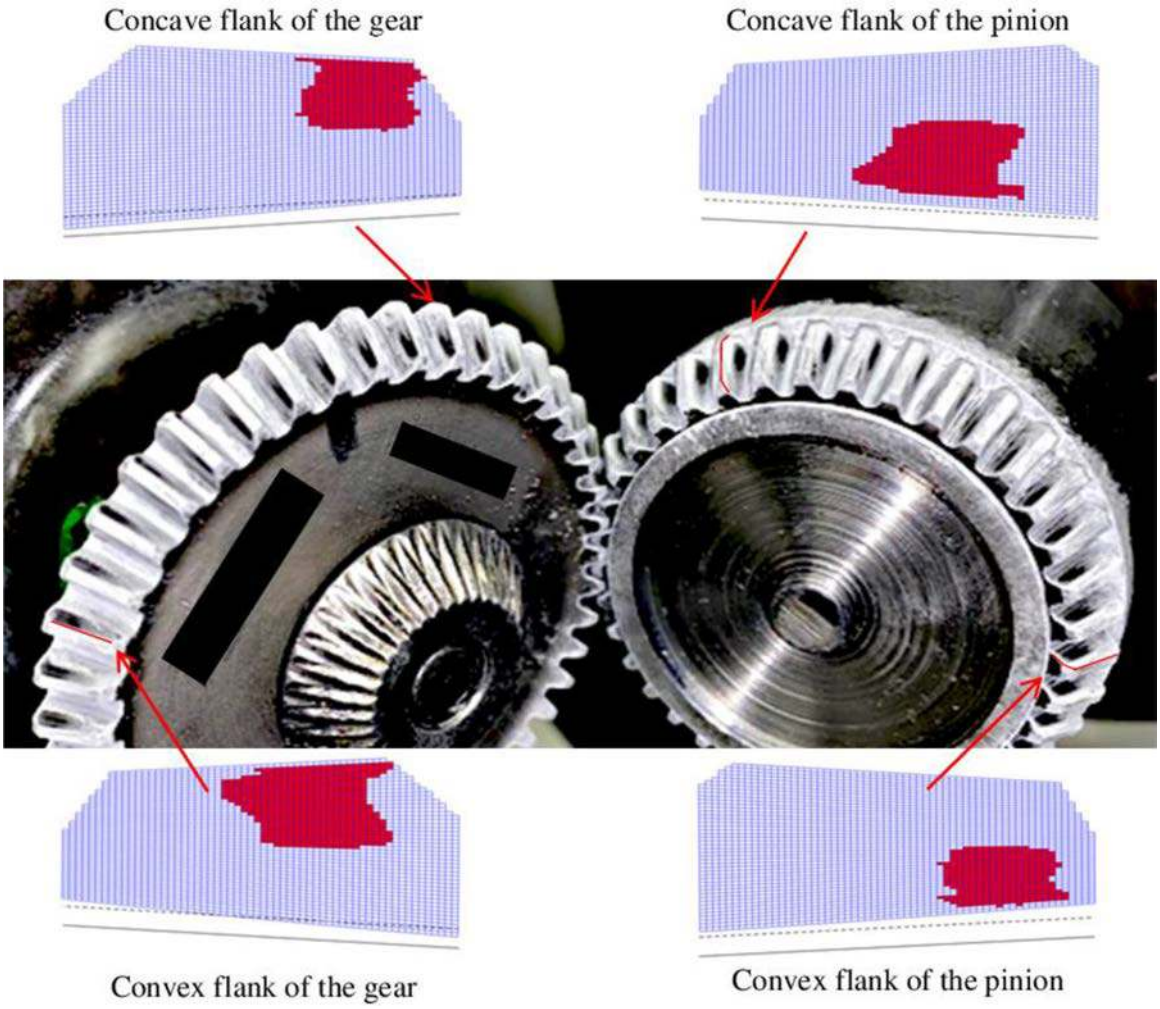

Fig. 11. Comparisons between numerical (4 drawings) and experimental (central photo) tooth contact patterns in configuration 1.

The stiffness matrix and forcing term vector associated with one contact stiffness element j are finally derived as:

$$\mathbf{k}_{\mathbf{ww}}^{Cj} = k_{Cj}\,\boldsymbol{\varphi}_{12j}\,\boldsymbol{\varphi}_{12j}^{T} \tag{20}$$

$$\mathbf{f}_{\mathbf{w}}^{Cj} = -k_{Cj}\,\delta e_j\,\boldsymbol{\varphi}_{12j} \tag{21}$$

2.5. Condensation of the equations of motion and time-step integration

Assuming that tooth eigenfrequencies are much higher than mesh frequency, their corresponding mode shapes can be discarded. Their contribution to inertia can therefore be included in the mass matrix of the rigid cones so that the equations of motion take the form [32]:

$$\begin{bmatrix} \mathbf{0} & \mathbf{0} \\ \mathbf{0} & \mathbf{M} \end{bmatrix} \begin{pmatrix} \ddot{\mathbf{w}} \\ \ddot{\mathbf{q}} \end{pmatrix} + \begin{bmatrix} \mathbf{0} & \mathbf{0} \\ \mathbf{0} & \mathbf{C} \end{bmatrix} \begin{pmatrix} \dot{\mathbf{w}} \\ \dot{\mathbf{q}} \end{pmatrix} + \begin{bmatrix} \mathbf{K}_{\mathbf{ww}} & \mathbf{K}_{\mathbf{qw}}^{T} \\ \mathbf{K}_{\mathbf{qw}} & \mathbf{K}_{\mathbf{qq}} \end{bmatrix} \begin{pmatrix} \mathbf{w} \\ \mathbf{q} \end{pmatrix} = \begin{pmatrix} \mathbf{F}_{\mathbf{w}} \\ \mathbf{F}_{\mathbf{q}} \end{pmatrix} \tag{22}$$

where:

$\mathbf{w}$ contains the nodal deflections for all active Pasternak foundations

$\mathbf{q}$ comprises all the degrees-of-freedom of the pinion and gear shafts

$\mathbf{M}$, $\mathbf{C}$ are the mass matrix and an approximate Rayleigh damping matrix

$\mathbf{F}_{\mathbf{q}}$ is a vector of external loads, including torque, excitations due to mounting deviations and additional loads on shafts

$\mathbf{F}_{\mathbf{w}}$ stems from the assembly of forcing term vectors $\mathbf{f}_{\mathbf{w}}^{Cj}$ of all pairs of cells in contact; it introduces the effect of initial tooth separations and is used to account for manufacturing and mounting deviations.

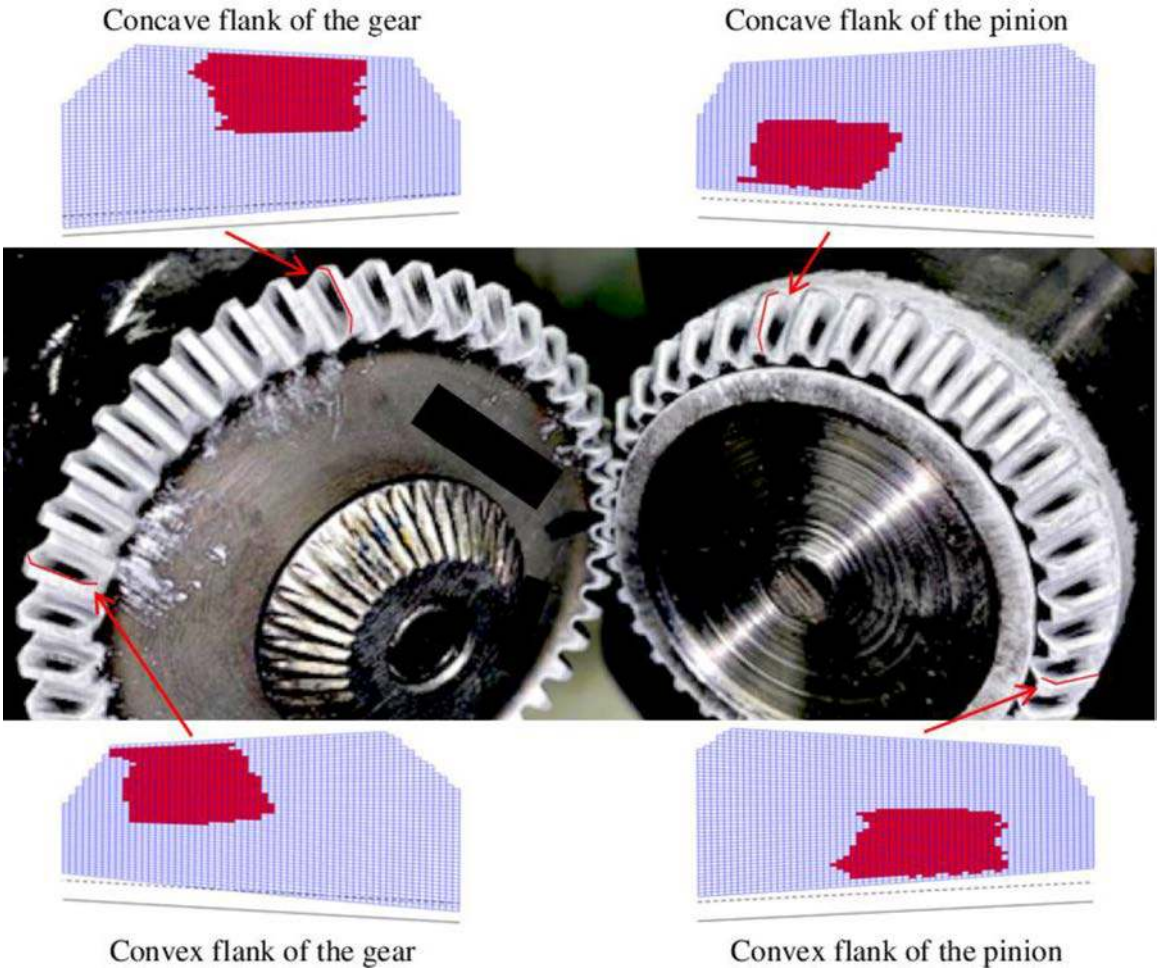

Fig. 12. Comparisons between numerical (4 drawings) and experimental (central photo) tooth contact patterns in configuration 2.

$\mathbf{K_{ww}}$ is derived by assembling the structural stiffness matrices $\mathbf{k_{ww}}$ of every foundation and the contact stiffness matrices $\mathbf{k}_{\mathbf{ww}}^{Cj}$ of each pair of cells in the contact patterns

$\mathbf{K_{qq}}$ is the assembly of the stiffness matrices of both shafts with their bearings and the stiffness matrices of foundation springs $\mathbf{k_{qq}}$

$\mathbf{K_{qw}}$ represents the couplings between rigid gear bodies and Pasternak foundations (assembling the matrices $\mathbf{k_{qw}}$ of each active foundations).

The damping matrix is expressed as $\mathbf{C} = \alpha\mathbf{M} + \beta\overline{\mathbf{K}}$, where $\overline{\mathbf{K}} = \int_0^{T_m} \mathbf{K}(t,\mathbf{w},\mathbf{q})\,dt$is the average stiffness matrix over one mesh period T_m. The two coefficients α and β are fitted over the frequency range of interest based on modal damping factors expressed as [36]$\xi_i \approx 0,07e_i + 0,01(1-e_i)$ with e_i, the percentage of modal strain energy stored in the tooth mesh.

Following [32], the deflections of the foundations are eliminated by substituting the first row of the system (22) in the second one, which yields:

$$\mathbf{M}\,\ddot{\mathbf{q}} + \mathbf{C}\,\dot{\mathbf{q}} + \mathbf{K}(t,\mathbf{w},\mathbf{q})\,\mathbf{q} = \mathbf{F}(t,\mathbf{w},\mathbf{q}) \tag{23}$$

where

$$\mathbf{K}(t,\mathbf{w},\mathbf{q}) = \mathbf{K_{qq}} - \mathbf{K_{qw}}\mathbf{K_w^{-1}}\mathbf{K_{qw}^{T}}$$

$$\mathbf{F}(t,\mathbf{w},\mathbf{q}) = \mathbf{F_q} - \mathbf{K_{qw}}\mathbf{K_{ww}^{-1}}\mathbf{F_w}$$

The solution procedure [35,37], Fig. 9) combines an implicit, unconditionally stable, Newmark scheme and a normal contact algorithm, which ensures that contact loads are compressive and that no interpenetrations occur outside the contact areas. At any time-step, the contact stiffness matrix is updated and the deflections of the Pasternak foundations are obtained after solving ((23). The

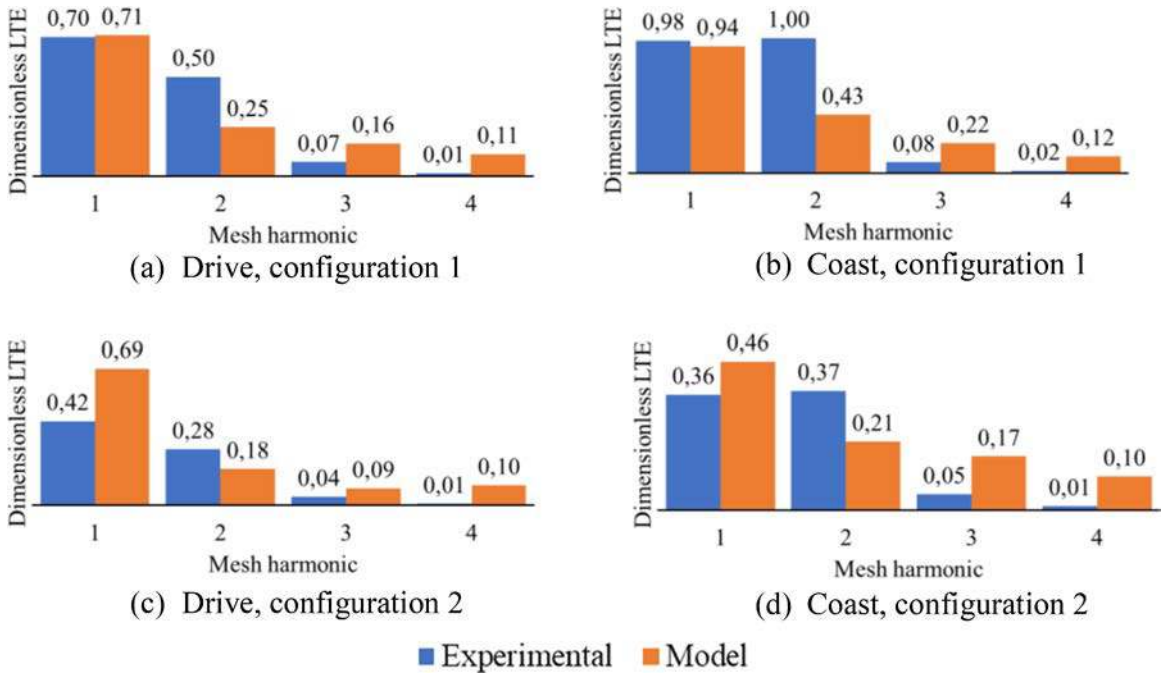

Fig. 13. Comparison between experimental and numerical transmission errors.

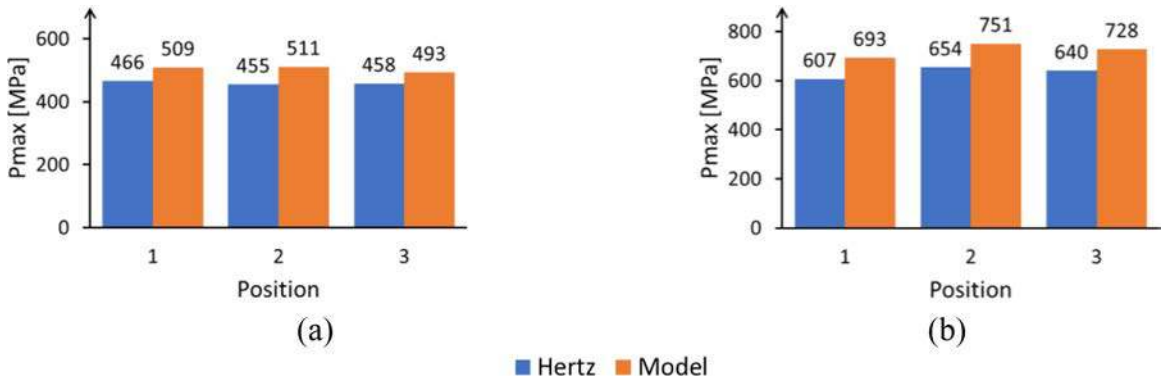

Fig. 14. Comparisons of maximal pressures by using the Hertzian theory and the foundation model; (a)Torque = 4 Nm; (b) Torque = 12 Nm.

process is repeated, based on updated deflections and sets of cells currently defining the contact zones on tooth flanks. Convergence is achieved when no pair of cells is added to or removed from the instant contact zones and when the variations in tooth deflections remain below a given threshold from one iteration to the next. Time is incremented and the process is repeated at the following time-step. A simulation over one mesh period (64 time-steps) using MATLAB® requires about 9 min CPU time on a desktop computer (processor i7 @ 2.60 GHz). Default parallelisation of matrix and array operations allows a shorter wall-clock time of about 2.5 min.

3. Elements of validation

The face-milled Zerol gear defined in Table 1 has been tested under load on a *Gleason 360T* single-flank tester with two combinations of assembly errors as defined in Fig. 10 i.e.,

(a) Axial positioning errors ΔP and ΔG on the pinion and gear (positively defined for displacements away from the intersection of the theoretical axes),
(b) Hypoid offset ΔE corresponding to a displacement perpendicular to the common plane of the theoretical axis of rotation,
(c) And a shaft angle increase $\Delta\Sigma$.

For the two configurations defined in Table 2, the pinion speed was 30 rpm and the gear torque 3 N.m. Measurements were

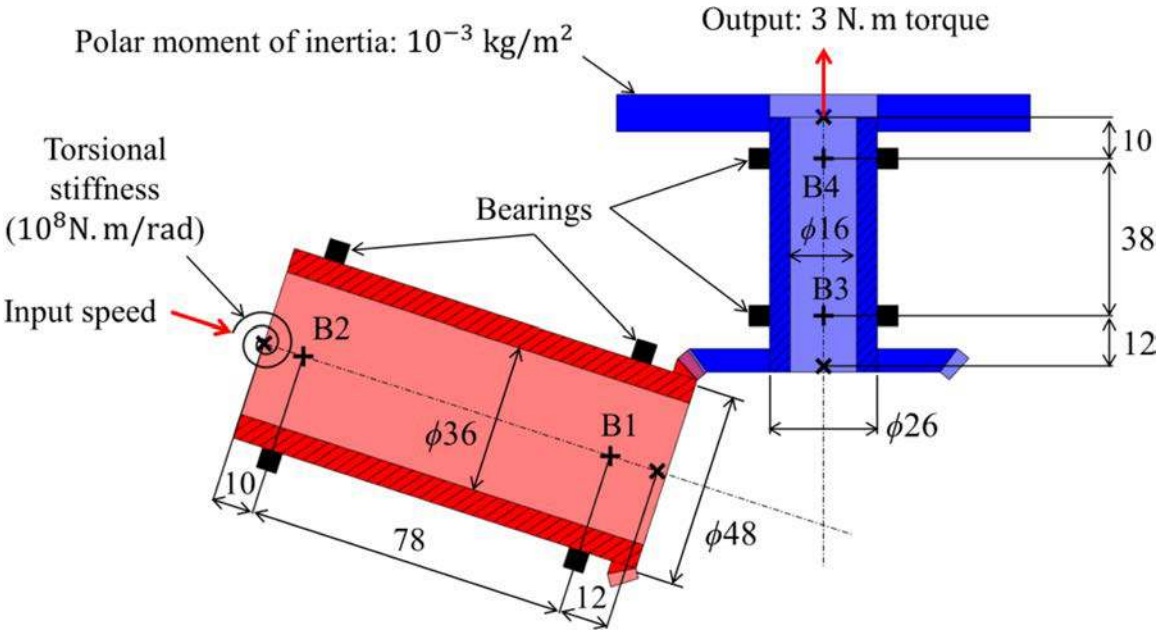

Fig. 15. Schematic representation of the system and boundary conditions (dimensions are expressed in mm).

Table 3
stiffness of bearings (off-diagonal elements are nil).

Bearings	$k_x = k_y$(radial)	k_z(axial)	$k_\phi = k_\psi$(bending)	k_θ(torsional)
B1, B3	10^8 Nm	10^8 Nm	10^5 Nm/rad	0 Nm/rad
B2, B4	10^8 Nm	0 Nm	10^5 Nm/rad	0 Nm/rad

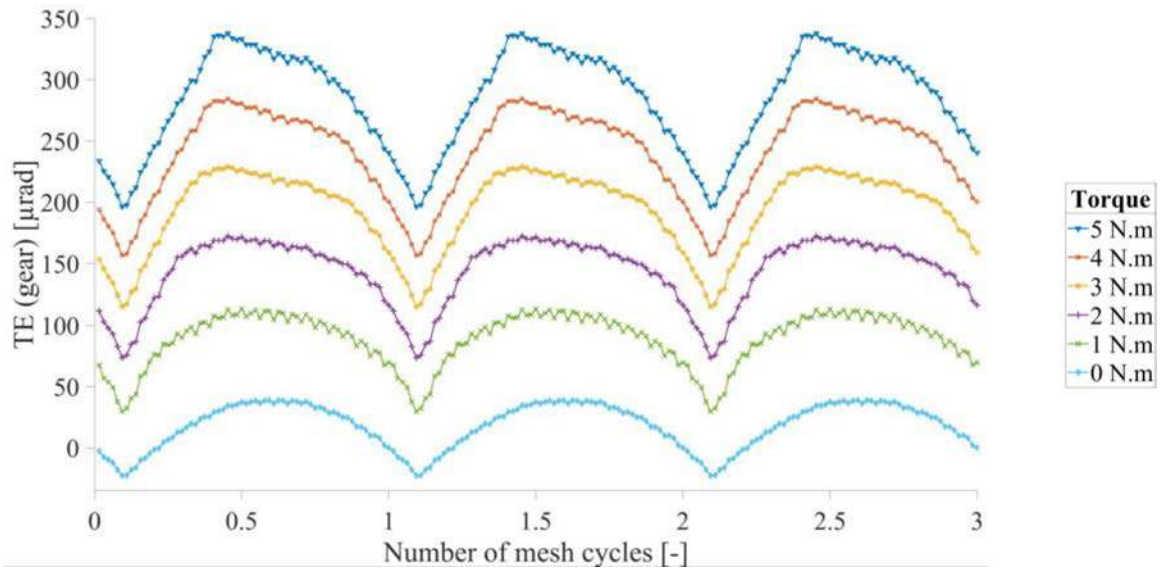

Fig. 16. Harris maps.

performed over 4 gear revolutions for the two directions of rotation, such that "coast" corresponds to the convex pinion flanks in contact with the concave gear flanks, whereas "drive" refers the pinion concave flanks meshing with the gear convex flanks. Optical encoders with 5946 slots per revolution were mounted on both spindles in order to measure transmission error under load. Finally, the envelopes of tooth contacts were estimated by using a white marking compound on the tooth surfaces, as per ANSI/AGMA 2008-D11.

Table 4
Transmission error and contact ratio at various loads.

Torque [Nm]	Mean value of TE [μrad]	Standard deviation of TE [μrad]	Contact ratio under load [-]
0	18	19	N/A
1	88	22	1.19
2	143	28	1.34
3	193	33	1.47
4	240	38	1.56
5	285	42	1.66

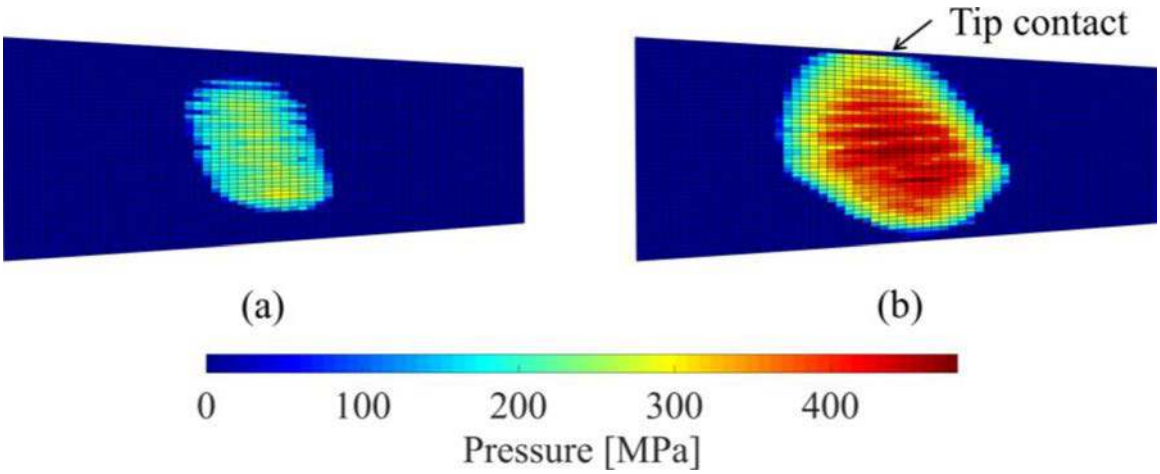

Fig. 17. Pressure distributions for a resistive torque of 1 Nm (a) and 5 Nm (b).

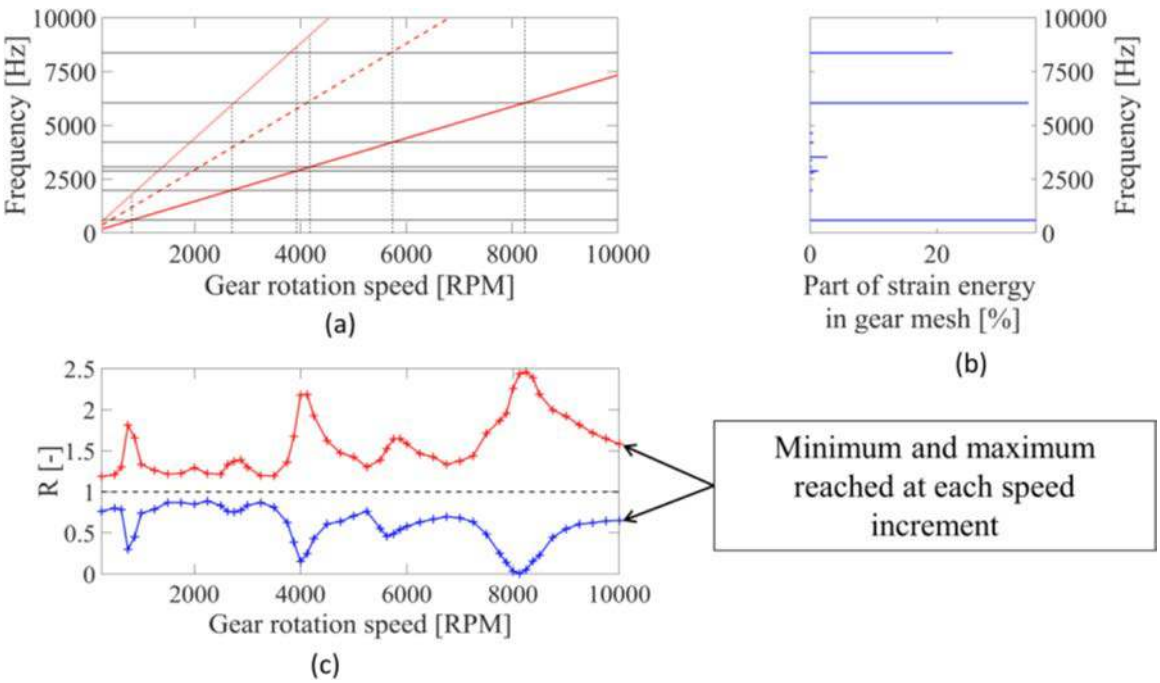

Fig. 18. Dynamic response; (a) Campbell diagram with the most significant modes; (b) mesh contribution to modal strain energy; (c) dynamic to static torque ratio.

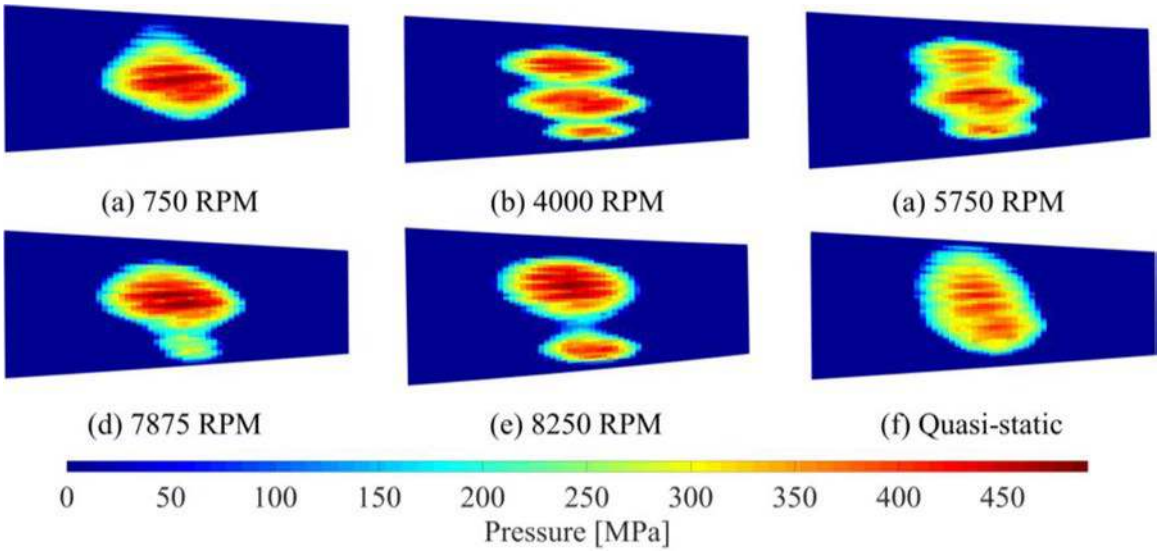

Fig. 19. Maximum pressure distributions at various speeds.

The surface deviations from nominal geometries were measured on a 19×19 point grid, averaged by considering three teeth located 120° apart and approximated by polynomial functions. The simulated contact patterns are deduced as the envelopes of the contact cells attached to one tooth submitted to positive contact forces between its engagement and end of recess. In these calculations, the thickness of the marking compound has been neglected. The darker stains in the photos below correspond to the experimental tooth contact patterns. In the model, all the teeth being the same and pitch errors being ignored, all teeth have identical loading conditions.

For the two senses of rotation, it can be observed in Figs. 11 and 12 that the numerical contact patterns agree well with the experimental ones for configurations 1 and 2. However, some tooth-to-tooth variations are visible on the measured contact areas. They are attributed to variations of the microgeometry, spacing errors and differences in the marking compound layer thickness and texture.

The experimental and numerical amplitudes of the 4 first mesh harmonics of transmission error under load are compared in Fig. 13 (*note that for confidentiality reasons, transmission error amplitudes have been normalized with respect to the maximum experimental amplitude*). The overall evolutions and amplitudes look comparable even if some discrepancies are reported for harmonic 2 in the 'coast' condition. The experimental time signals (not shown) are clearly dominated by the low-frequency components associated with runout and pitch errors, which were not included in the model. The differences between the experimental evidence and the simulation results can predominantly be attributed to the averaged tooth geometry employed (see above) and to the fact that tooth geometries were extrapolated near their edges since the tooth surfaces measured did not cover the entire flanks. For these reasons, the theoretical surfaces may slightly depart from the actual ones, particularly near the edges where local tooth shape modifications (tribo-finishing) could be significant. However, in spite of these uncertainties, the overall agreement between the experimental and numerical results is deemed acceptable.

A final set of comparisons is shown in Fig. 14 where, for three angular positions and two torque levels, the maximum contact pressures derived from the fine grid are confronted with those given by the Hertzian theory. In the model, the pressure is supposed to be uniform over each contact cell and is estimated by multiplying the interpenetration by the local contact stiffness and then dividing by the cell surface area. The derivation of the Hertzian pressure is briefly summarised in annex C. Here again, the two sets of results compare well. Overall, the agreement between the simulations results and the evidence from the test rig or classic results from the literature appears as satisfactory, thus validating the proposed mesh interface model.

4. Quasi-static and dynamic results

4.1. Model

To illustrate the applicability of the model, an academic test-case has been created based on the pinion and gear used in the experimental validation (Section 3). The nominal tooth geometry is considered and a simplified shaft-bearing model is introduced with no assembly errors as illustrated in Fig. 15.

All parts are made of steel ($\rho = 7850\,\mathrm{kg/m^3}$, $E = 200\,\mathrm{GPa}$, $\nu = 0{,}3$) and each shaft is supported by two bearings, represented by constant and diagonal stiffness matrices (Table 3). The end of the pinion shaft is connected to the input by means of a torsional spring, authorizing small rotations around the prescribed rigid body positions. A resisting torque is applied at the last node of the gear shaft and a polar inertia is added to simulate the driven member. The direction of rotation is chosen such that the contacts are on coast flanks.

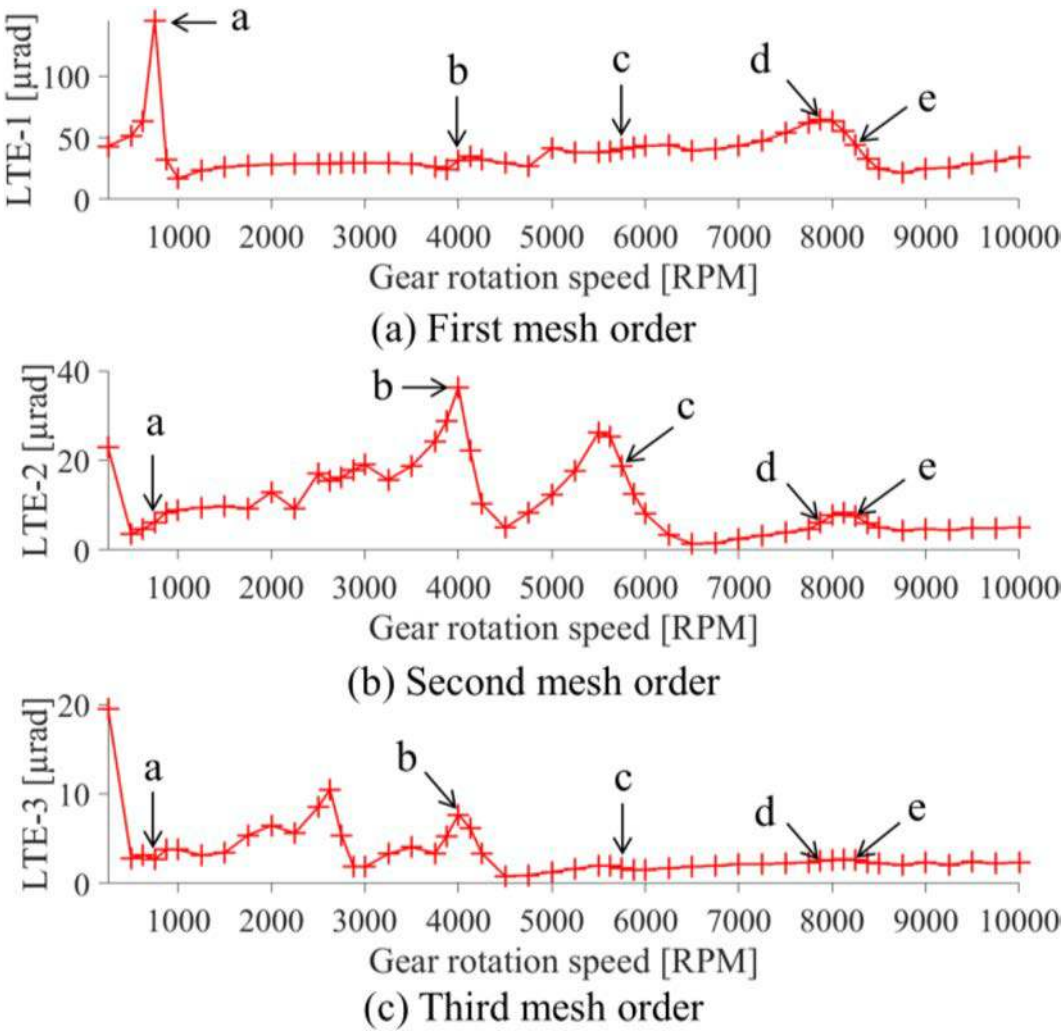

Fig. 20. Transmission error versus speed for the three first mesh orders.

4.2. Effect of torque on quasi-static behaviour

The simulated time-variations of quasi-static transmission error (TEs) are plotted in Fig. 16 for six torque levels (Harris map), which show that both the mean values and amplitudes increase with load, thus indicating that the tooth geometries, in this example, were not optimised with regard to TEs.

Defining the total contact ratio as the average number of tooth pairs with at least one loaded cell over the course of the simulation, it can be observed in Table 4 that it is highly sensitive to torque and significantly increases with the transmitted load. For the sake of comparison, the corresponding contact ratio according to ISO 10300–1:2014(E) is 1.54, which is an approximate value calculated at tooth half-width on an equivalent spur gear and matches with the simulation results around the nominal torque.

This sensitivity of the contact properties to load is also illustrated by the results in Fig. 17, which reveal that the envelope of the contact zones on pinion flanks become substantially larger with load. It can be noticed that corner contacts at the pinion tooth tips are beginning to appear at the highest load, suggesting that it is not beneficial to go beyond a 5 Nm torque in this example.

4.3. Dynamic analysis

Considering the modes with the highest percentages of modal strain energy stored in the tooth mesh, Fig. 18 (a, b) shows the corresponding Campbell diagram when excitations are supposed to be represented by the first three harmonics of mesh frequency only (the natural frequencies were determined by using the averaged quasi-static mesh stiffness). Based on the results of time-step integrations, the maximum (R_{max}) and minimum (R_{min}) dynamic to static mesh torque ratios have been derived in Fig. 18(c), for speeds up to 10 000 rpm on the gear shaft and a constant gear torque of 3 Nm. Five main resonance peaks are observed over the speed range, for which dynamic mesh forces are amplified. It is also confirmed that the dynamic response curve structure is controlled by the

coincidences between the critical natural frequency with regard to mesh strain energy and the mesh excitation frequencies, in line with the findings for spur and helical gears [38,39].

The maximum pressure distributions at each of the critical speeds in Fig. 19 show that the dynamic contact patterns depart largely from that in quasi-static conditions and that clear dynamic effects emerge since speed appears as highly influential. The maximum pressure distribution at the major critical speed for R_{max} (8250 rpm) reveals that the contact on one flank is almost intermittent since pressures close to zero are obtained (see also the corresponding R_{min} in Fig. 18(c)). For this major response peak (Fig. 19(e)), the maximum dynamic pressure reaches 491 MPa, compared with a quasi-static amplitude of 420 MPa (Fig. 19(f)).

Dynamic transmission error is another outcome of interest. Its amplitudes by mesh order (first 3 harmonics) are plotted versus speed in Fig. 20, where labels *a* to *e* refer to the speed at which the dynamic pressure distributions in Fig. 19 have been calculated. It can be noticed that each harmonic contributes differently to the overall signal. For resonances *(a)* and *(d)*, the first mesh harmonic dominates and the corresponding contact patterns consist in rather uniform patches on tooth flanks. For other resonances, higher order harmonics are involved and several loaded sub-zones appear on the pressure distributions. Particularly, resonance *(b)* with mesh order amplitudes of 31 μrad, 36 μrad and 8 μrad, respectively, is characterized by three distinct pressure spots. These results illustrate the interactions between the local (tooth contacts) and global (transmission error) scales and emphasize the interest of solving the equations of motion and contact problem simultaneously.

5. Conclusion

An original model of bevel gears has been presented, which, in contrast with the majority of those found in the literature, can be employed for both quasi-static and dynamic analyzes. Its main characteristics are:

(a) An enhanced mesh elasticity model including elastic couplings based on a unique combination of Pasternak foundations for tooth structural deflections and time-varying non-linear Winkler foundations for contacts.
(b) The capability to simultaneously solve the equations of motion and the normal contact problem between tooth flanks step-by-step in time. No a-priori hypotheses on the contact locations are required and actual tooth flank topographies and assembly errors can be included.

The resulting numerical transmission errors and contact patterns compare well with experimental evidence obtained at low speeds, thus validating the mesh interface model. A series of dynamic results have been presented, which illustrate the capacity of the proposed model to simulate the contact conditions but also shaft-bearing behavior at high-speeds. It has been shown, in particular, that dynamic couplings can be expected between the local scale associated with tooth contacts and the global scale of the complete mechanism, since dynamic contact zones are dependant on modal contents. With regard to computational efficiency, simulations over several pinion or gear revolutions are possible within a small fraction of the time required by non-linear 3D finite element calculations, thus making it possible to perform extended parameter analyzes.

As it stands, simulations are limited to straight and spiral bevel gears but extensions to hypoid gears seem straightforward. Further research is currently under way in order to combine the proposed mesh interface model with substructures in order to account for more complex and realistic mechanical transmissions.

Declaration of Competing Interest

None.

Acknowledgments

The authors would like to thank SAFRAN Helicopter Engines (SAFRAN group) and the ANRT (French National Association for Research and Technology), for their support via a CIFRE grant attributed to Mr. Augustin Pigé.

Annex A: Identification of foundation parameters

The procedure to identify the parameters of the discrete Pasternak's foundation, i.e. stiffness k_{ii} (at each node) and shear coefficients G_j for each element is described. Instead of looking for the total number of discrete values, bilinear Lagrange's interpolation over the tooth mid-surface is used such that:

$$\langle k_{11} \quad \cdots \quad k_{nn} \rangle^T = k_{ini} \mathbf{L_k} \widehat{\mathbf{k}} \tag{A1}$$

$$\langle G_1 \quad \cdots \quad G_m \rangle^T = G_{ini} \mathbf{L_G} \widehat{\mathbf{G}} \tag{A2}$$

where matrices $\mathbf{L_k}$ and $\mathbf{L_G}$ contain the values of the Lagrange polynomial at each node and at the centroid of each element, respectively. The optimisation variables stored in vectors $\widehat{\mathbf{k}}$ and $\widehat{\mathbf{G}}$ correspond to the values of stiffness and of shear parameters normalised with respect to k_{ini} and G_{ini} at regularly spaced points on tooth mid-surface. The stiffness k_{ini} is defined by the bending deflection of a clamped-free thin beam and G_{ini} is the shear coefficient of the Pasternak foundation representing an elastic layer of constant thickness [29]. The beam dimensions and elastic layer thickness are based on the average dimensions of the actual tooth.

It has been found that the following polynomial approximations are precise enough: a) order 0 to 2 along tooth width and, b) in the tooth height direction, order 3 to 4 for the stiffness coefficients and order 2 to 3 for the shear coefficients. The total number of unknowns therefore lies between 7 and 27. As stiffness decreases relatively rapidly along tooth height, matrix $\mathbf{L_k}$ is often modified to interpolate the stiffness on the lowest rows of nodes and set to 0 the stiffness of the springs close to tooth tips.

An objective function is introduced, which is a measure of the deviation between the solutions given by a model of reference and the Pasternak's foundation. Models of reference for tooth structural deflections can either be the shell model in [3] or a 3D finite element model as illustrated in Fig. A1, so that static gear-body contributions can be included. The following procedure is then applied:

(1) calculate the stiffness of every springs and the shear coefficient of each surface element of the foundation using Eqs. (A1) and (A2)
(2) assemble the stiffness matrix of the foundation, based on dimensionless elemental stiffness matrices computed once before optimisation
(3) solve for the deflections obtained when considering several loading conditions; for instance, constant pressure distributions (Fig. A2) over ten distinct zones covering the entire tooth surface

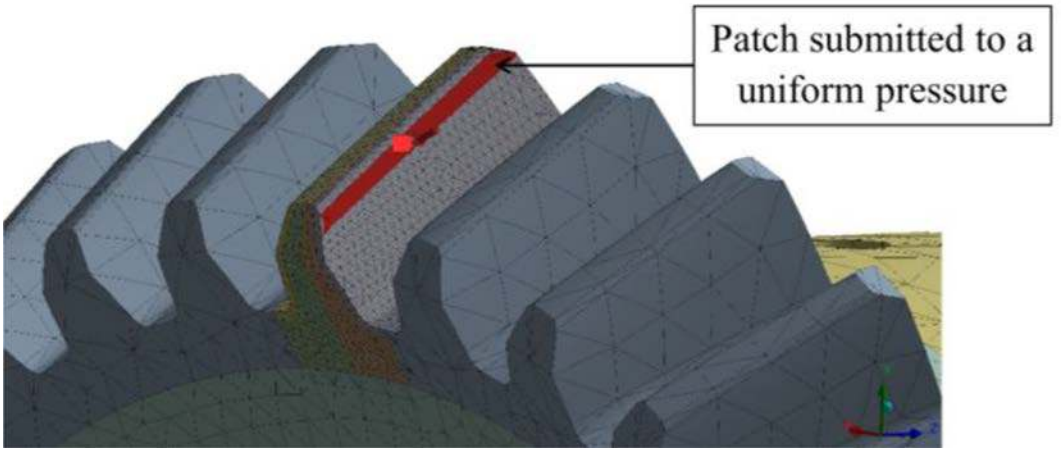

Fig. A1. Finite element model used as a reference - example of loading condition.

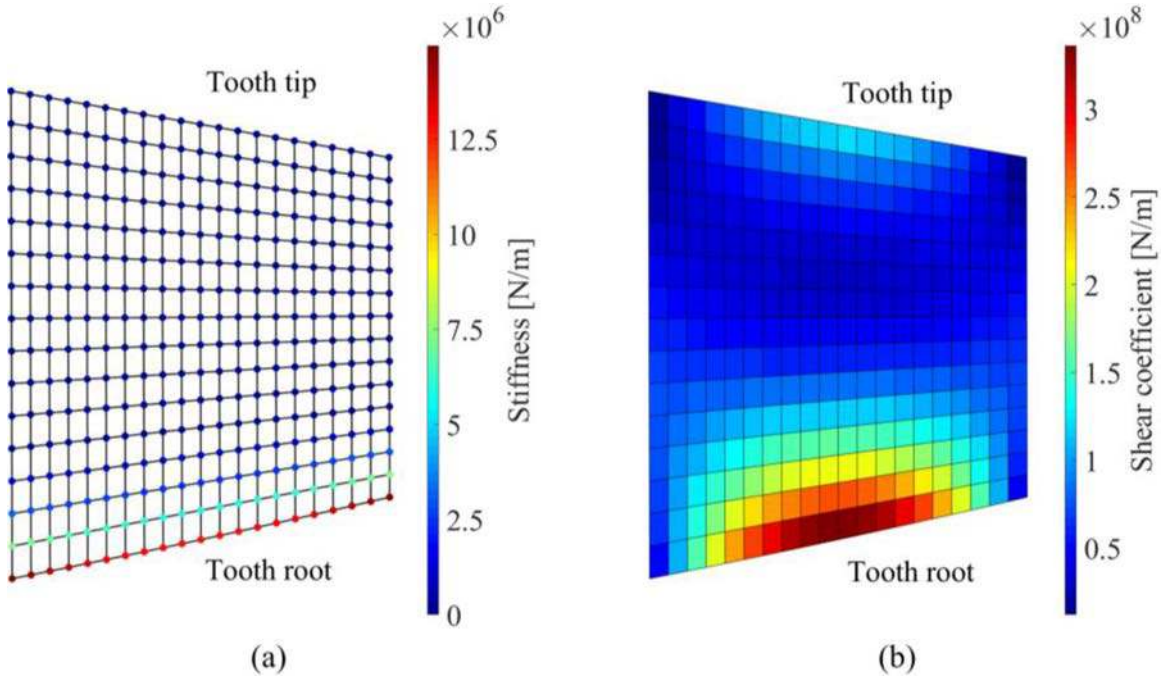

Fig. A2. Example of identified foundation parameters: (a) stiffness of springs; (b) shear coefficient of elements.

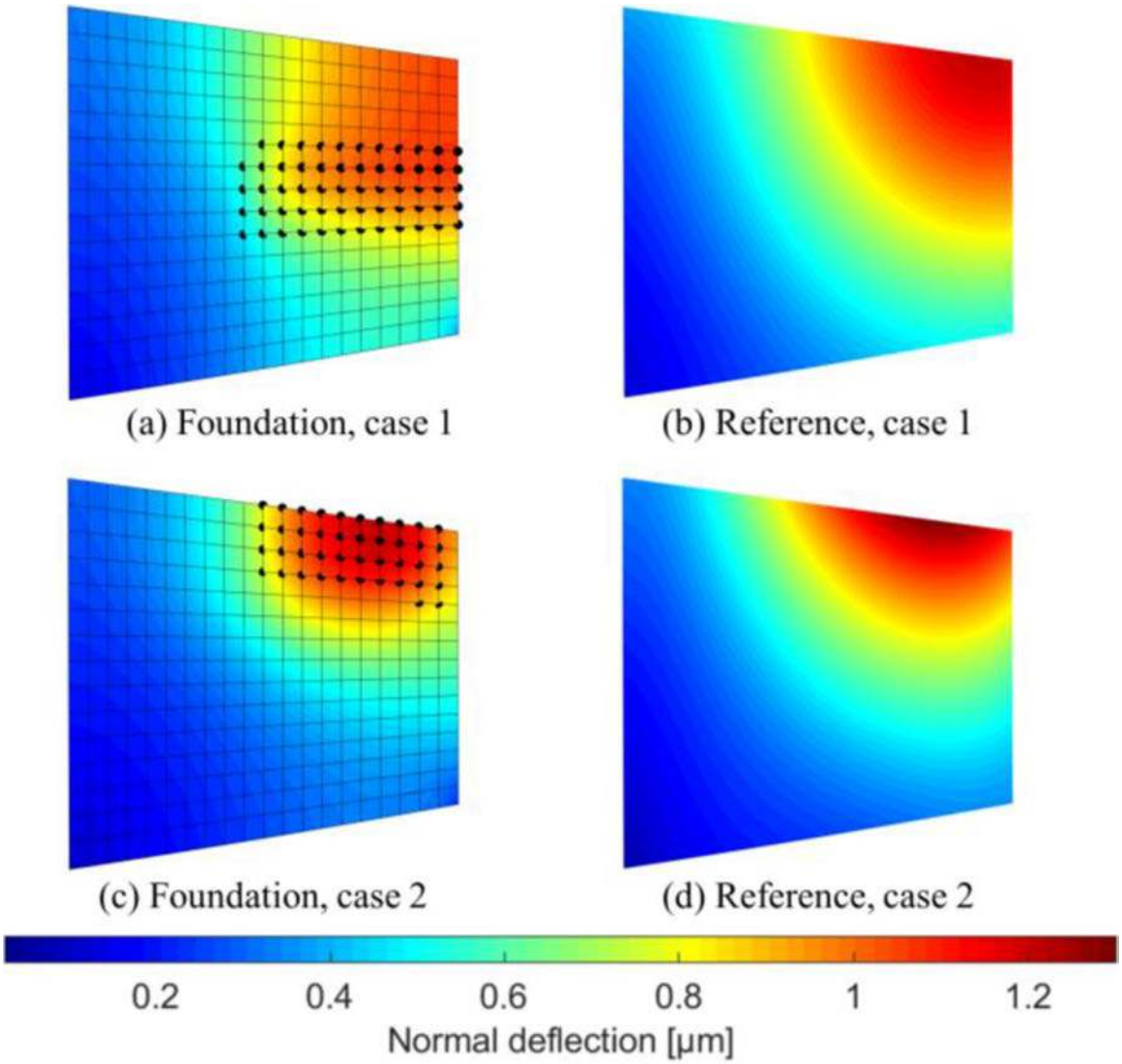

Fig. A3. Comparisons between the deflections of the Pasternak's foundation and those given by the 3-dimensionnal model of reference. Black dots indicate the loaded nodes on the foundation model.

(4) evaluate the overall deviation between the reference and foundation models as a weighted sum of squared errors at all the nodes and for all the loading conditions

The pattern search algorithm in MATLAB® is employed to iteratively solve this optimisation problem [40].

An example of identification results is given in Fig. A2 (stiffness at nodes and shear coefficient constant over a surface element). Here, the stiffness of springs placed at nodes of the six highest rows is set to zero. The solution of reference is derived from a finite element model including the gear body and all teeth (Fig. A1). It can be verified in Fig. A3 that, for two loading cases, the deflections obtained using the Pasternak's foundation and those given by the reference model are in good agreement.

Annex B: Elastic half-space coefficients of influence

Contact deflections are approximated by the convolution of Boussinesq's solution for an infinite half-space submitted to a point load with a pressure distribution $p(x',y')$ over its surface (S)[9], [34]:

$$w_B(x,y,z) = \frac{1+\nu}{2\pi E}\int_{(s)} p(x',y')\left[\frac{z^2}{r(x',y',x,y,z)^3}+\frac{2(1-\nu)}{r(x',y',x,y,z)}\right]dx'dy' \tag{B1}$$

with the distance: $r(x',y',x,y,z) = \sqrt{(x-x')^2+(y-y')^2+z^2}$

Tooth flanks are discretized into rectangles of dimensions $2a$ and $2b$ over which pressures are considered as uniform. In what follows, the centre of cell i is the origin of a rectangular frame (Fig. B1). This cell is submitted to a uniformly distributed force F_i while the others remain free. The deflection at the surface reads [9]:

$$w_B(x,y,0) = \frac{1-\nu^2}{\pi E}\frac{F_i}{4ab}\left[\left(Y\operatorname{arcsh}\left(\frac{X}{|Y|}\right)+X\operatorname{arcsh}\left(\frac{Y}{|X|}\right)\right)_{X=x-a}^{X=x+a}\right]_{Y=y-b}^{Y=y+b} \tag{B2}$$

Since contact deflections are added to the structural ones, they should vanish on tooth mid-surfaces, where the latter are computed [9,34]. Therefore, the deflections of the elastic half space at a depth corresponding to tooth mid-surface are subtracted from Eq. (B2). While the typical order of magnitude of this depth varies from 1 mm to 1 cm, an accurate contact detection requires cells to be about one tenth of a millimetre long. Hence:

$$z \gg |x'| \text{ and } z \gg |y'| \tag{B3}$$

As contact convectivity is spatially more limited than structural convectivity, the calculations of influence coefficients are restricted to closely neighbouring cells. One can therefore assume:

$$z^2 \gg |xx'| \text{ and } z^2 \gg |yy'| \tag{B4}$$

Using these conditions in (B1) yields:

$$w_B(x,y,z) \approx \frac{1+\nu}{2\pi E}F_i\left[\frac{z^2}{(x^2+y^2+z^2)^{3/2}}+\frac{2(1-\nu)}{\sqrt{x^2+y^2+z^2}}\right] \tag{B5}$$

and the influence coefficient is derived as:

$$C_{mij} = \left[w_B(x_{ij},y_{ij},0) - w_B(x_{ij},y_{ij},z_j)\right] / F_i \tag{B6}$$

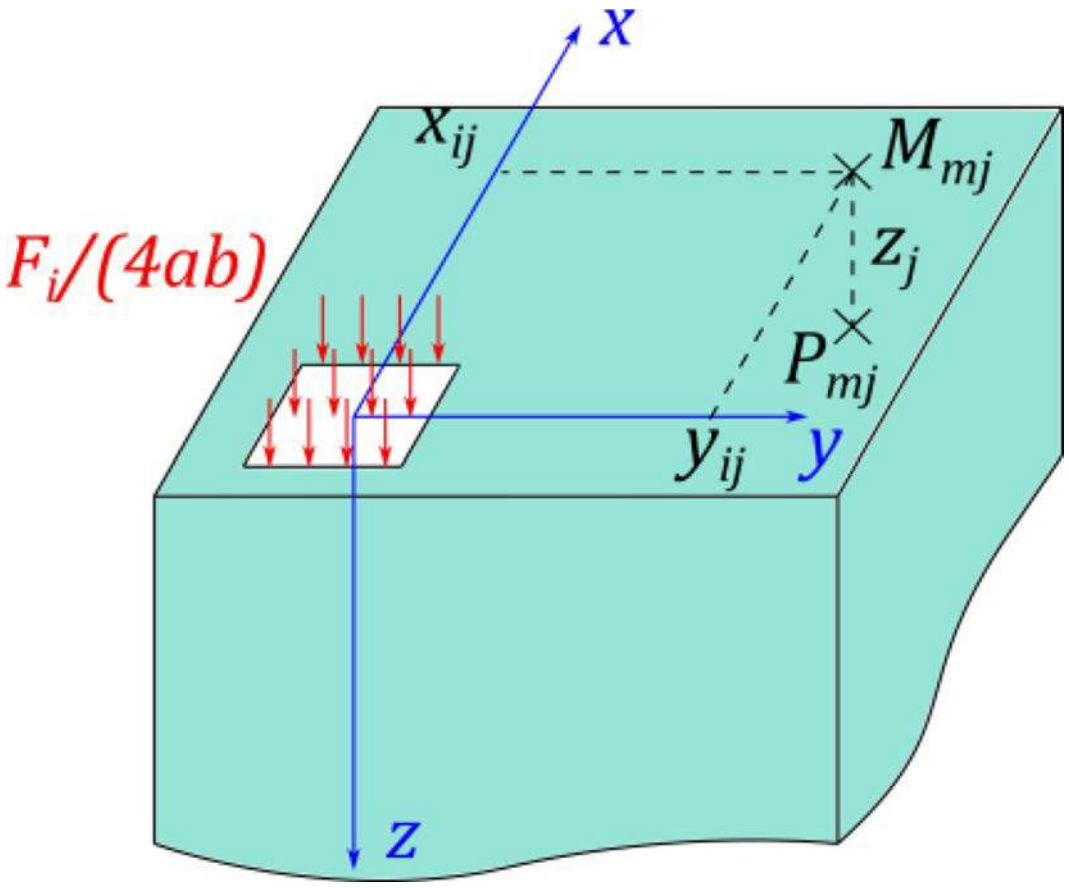

Fig. B1. infinite half-space.

where index m relates to the pinion (1) or to the gear (2) and z_j is the depth below cell j, where the deflection is evaluated.

Annex C: derivation of Hertzian pressure

The point of contact in rigid body conditions is used as the datum for separations. The orthogonal vectors **x**and **y** are tangent to the contact cell of this point. They are used to express the relative coordinates (x, y) of the neighbouring cell centres. Using a least-square method, the gaps in rigid-body conditions are approximated as $\delta e = \alpha x^2 + \beta y^2 + \gamma xy$. The curvatures of this surface correspond to the relative curvatures of the mating flanks derived by defining a normal vector:

$$\mathbf{N} = \left\langle \frac{\partial \delta e}{\partial x} \quad \frac{\partial \delta e}{\partial y} \quad -1 \right\rangle^T = \langle\, 2\alpha x + \gamma y \quad 2\beta y + \gamma x \quad -1 \,\rangle^T \tag{C1}$$

The differential of the Gaussian mapping ($\mathbf{N}/\parallel \mathbf{N} \parallel$) [41] at the point of contact in rigid body conditions reads:

$$\mathbf{dn}(0,0) = \begin{bmatrix} 2\alpha & \gamma \\ \gamma & 2\beta \end{bmatrix} \tag{C2}$$

The mean curvature H_p and Gaussian curvature K_p are derived as [41]:

$$H_p = \frac{1}{2}\mathrm{tr}(\mathbf{dn}) = \alpha + \beta \text{ and } K_p = det(\mathbf{dn}) = 4\alpha\beta - \gamma^2 \tag{C3}$$

These relations between trace, determinant, mean and Gaussian curvatures also hold true in the basis of principal curvatures. The minimum and maximum curvatures are therefore:

$$k_1 = H_p + \sqrt{H_p^2 - K_p} \text{ and } k_2 = H_p - \sqrt{H_p^2 - K_p} \tag{C4}$$

An equivalent radius of relative curvature is introduced as [42]:

$$R_e = 1/\sqrt{K_p} \tag{C5}$$

Hertzian theory assumes that the contact zone is an ellipse of semi-major axis a and semi-minor axis b. The aspect ratio a/b of the ellipse must satisfy [42]:

$$\frac{k_1}{k_2} = \frac{(a/b)^2 E(e) - K(e)}{K(e) - E(e)} \tag{C6}$$

where E and K are complete elliptic integrals of eccentricity: $e = \sqrt{1 - (b/a)^2}$. Eq. (C6) is solved approximately by sweeping over a range of aspect ratios. Elliptic integrals are interpolated from tables in [43]. Then, parameter $F_1(e)$ is calculated:

$$F_1(e) = \left(\frac{4}{\pi e^2}\right)^{1/3} \left(\frac{b}{a}\right)^{1/2} \left\{ \left[\left(\frac{a}{b}\right)^2 E(e) - K(e) \right] [K(e) - E(e)] \right\}^{1/6} \tag{C7}$$

Hertzian pressures are to be compared with the pressures determined by the proposed model at given positions. Only the time-steps when a single tooth-pair is in mesh are considered to avoid load-sharing calculations. Hence, forces transmitted through each contact pair are added up in the total force F. Finally, the maximum pressure is [42]:

$$p_0 = \left(\frac{6FE^{*2}}{\pi^3 R_e^2}\right)^{1/3} [F_1(e)]^{-\frac{2}{3}} \tag{C8}$$

where E^* is the equivalent Young's modulus:

$$\frac{1}{E^*} = \frac{1 - \nu_1^2}{E_1} + \frac{1 - \nu_2^2}{E_2} \tag{C9}$$

References

[1] F.L. Litvin, A. Fuentes, Gear Geometry and Applied Theory, 2nd ed., Cambridge University Press, 2004.

[2] J. Argyris, A. Fuentes, F.L. Litvin, Computerized integrated approach for design and stress analysis of spiral bevel gears, Comput. Methods Appl. Mech. Eng. 191 (11–12) (2002) 1057–1095, https://doi.org/10.1016/S0045-7825(01)00316-4.

[3] M. Kolivand, A. Kahraman, A load distribution model for hypoid gears using ease-off topography and shell theory, Mech. Mach. Theory 44 (10) (2009) 1848–1865, https://doi.org/10.1016/j.mechmachtheory.2009.03.009.

[4] M. Kolivand, H. Ligata, G. Steyer, D.K. Benedict, J. Chen, Actual tooth contact analysis of straight bevel gears, J. Mech. Des. 137 (9) (2015), https://doi.org/10.1115/1.4031025.

[5] M. Vivet, D. Mundo, T. Tamarozzi, W. Desmet, An analytical model for accurate and numerically efficient tooth contact analysis under load, applied to face-milled spiral bevel gears, Mech. Mach. Theory 130 (2018) 137–156, https://doi.org/10.1016/j.mechmachtheory.2018.08.016.

[6] M. Vivet, T. Tamarozzi, W. Desmet, D. Mundo, On the modelling of gear alignment errors in the tooth contact analysis of spiral bevel gears, Mech. Mach. Theory 155 (2021), https://doi.org/10.1016/j.mechmachtheory.2018.08.016.
[7] M.A. Hotait, A. Kahraman, T. Nishino, An investigation of root stresses of hypoid gears with misalignments, J. Mech. Des. 133 (7) (2011), https://doi.org/10.1115/1.4004224.
[8] H. Ding, J. Tang, J. Zhong, Z. Zhou, A hybrid modification approach of machine-tool setting considering high tooth contact performance in spiral bevel and hypoid gears, J. Manuf. Syst. 41 (2016) 228–238, https://doi.org/10.1016/j.jmsy.2016.09.003.
[9] S. Vijayakar, A combined surface integral and finite element solution for a three-dimensional contact problem, Int. J. Numer. Methods Eng. 31 (3) (1991), https://doi.org/10.1002/nme.1620310308.
[10] C. Gosselin, L. Cloutier, Q.D. Nguyen, A general formulation for the calculation of the load sharing and transmission error under load of spiral bevel and hypoid gears, Mech. Mach. Theory 30 (3) (1995) 433–450, https://doi.org/10.1016/0094-114X(94)00049-Q.
[11] V. Simon, Design of face-hobbed spiral bevel gears with reduced maximum tooth contact pressure and transmission errors, Chin. J. Aeronaut. 26 (3) (2013) 777–790, https://doi.org/10.1016/j.cja.2013.05.005.
[12] V. Simon, Load distribution in spiral bevel gears, J. Mech. Des. 129 (2) (2007) 201–209, https://doi.org/10.1115/1.2406090.
[13] J.P. de Vaujany, M. Guingand, D. Remond, Y. Icard, Numerical and experimental study of the loaded transmission error of a spiral bevel gear, J. Mech. Des. 129 (2) (2006) 195–200, https://doi.org/10.1115/1.2406089.
[14] S. Vaidyanathan, H.R. Busby, D.R. Houser, A numerical approach to the static analysis of an annular sector Mindlin plate with applications to bevel gear design, Comput. Struct. 51 (3) (1994) 255–266, https://doi.org/10.1016/0045-7949(94)90333-6.
[15] C. Gosselin, P. Gagnon, L. Cloutier, Accurate tooth stiffness of spiral bevel gear teeth by the finite strip method, J. Mech. Des. 120 (4) (1998), https://doi.org/10.1115/1.2829321.
[16] W. Wagner, S. Schumann, B. Schlecht, Co-simulation of the tooth contact of bevel gears within a multibody simulation, Forsch. Ingenieurwes 83 (3) (2019) 425–433, https://doi.org/10.1007/S10010-019-00360-7.
[17] D.B. Dooner, M. Vivet, D. Mundo, Deproximating tredgold's approximation, Mech. Mach. Theory (102) (2016) 36–54, https://doi.org/10.1016/j.mechmachtheory.2016.03.004.
[18] D.G. Astridge, M. Salzer, Gearbox dynamics: modelling of a spiral bevel gearbox, in: Proceedings of the Third European Rotorcraft and Power Lift Aircraft Conference, 1977, pp. 1–10.
[19] Y. Cheng, T.C. Lim, Vibration analysis of hypoid transmissions applying an exact geometry-based gear mesh theory, J. Sound Vib. 240 (3) (2001) 519–543, https://doi.org/10.1006/jsvi.2000.3247.
[20] Y. Cheng, T.C. Lim, Dynamics of hypoid gear transmission with nonlinear time-varying mesh characteristics, J. Mech. Des. 125 (2) (2003) 373–382, https://doi.org/10.1115/1.1564064.
[21] N. Sainte-Marie, A Transmission-Error-Based Gear Dynamic model: Applications to single- and multi-Mesh Transmissions, Université de Lyon, 2016. PhD. thesis.
[22] J.J. Yang, Z.H. Shi, H. Zhang, T.X. Li, S.W. Nie, B.Y. Wei, Dynamic analysis of spiral bevel and hypoid gears with high-order transmission errors, J. Sound Vib. 417 (2018) 149–164, https://doi.org/10.1016/j.jsv.2017.12.022.
[23] S.D. Yavuz, Z.B. Saribay, E. Cigeroglu, Nonlinear time-varying dynamic analysis of a spiral bevel geared system, Nonlinear Dyn. 92 (4) (2018) 1901–1919, https://doi.org/10.1007/S11071-018-4170-9.
[24] J. Yang, T.C. Lim, Nonlinear dynamic simulation of hypoid gearbox with elastic housing, in: Proceedings of the International Design Engineering Technical Conferences and Computers and Information in Engineering Conference 54853, 2011, pp. 437–447.
[25] Y. Wang, X. Li, G. Qiao, T. Lim, Effect of component flexibility on axle system dynamics, SAE Int. J. Veh. Dyn. Stab. NVH 1 (2017) 400–407, https://doi.org/10.4271/2017-01-1772.
[26] Y. Wang, T.C. Lim, J. Yang, Multi-point mesh modeling and nonlinear multi-body dynamics of hypoid geared system, SAE Int. J. Passeng. Cars Mech. Syst. 6 (2013) 1127–1132, https://doi.org/10.4271/2013-01-1895.
[27] T. Peng, Coupled Multi-Body Dynamic and Vibration Analysis of Hypoid and Bevel Geared Rotor System, University of Cincinnati, 2010. PhD. thesis.
[28] Q. Thoret-Bauchet, Simulations Du Comportement Vibratoire De Réducteurs D'entraînement Pour Machine Outil - Applications à la Détection Et à L'identification De Défauts, Université de Lyon, 2020.
[29] A.D. Kerr, On the determination of foundation model parameters, J. Geotech. Eng. 111 (11) (1985) 1334–1340, https://doi.org/10.1061/(ASCE)0733-9410(1985)111:11(1334).
[30] D.L. Seager, Some Elastic Effects in Helical Gear Teeth, University of Cambridge, 1967. PhD. thesis.
[31] G.R. Schmidt, W. Pinnekamp, A. Wunder, Optimum tooth profile correction of helical gears, in: Proceedings of the 3rd International Power Transmissions and Gearing Conference, 1980.
[32] M. Ajmi, P. Velex, A model for simulating the quasi-static and dynamic behavior of solid wide-faced spur and helical gears, Mech. Mach. Theory 40 (2) (2005) 173–190, https://doi.org/10.1016/j.mechmachtheory.2003.06.001.
[33] C. Weber, The Deformations of Loaded Gears and Their Effects On Their Load-Carrying capacity (no. 3) (1949). Report.
[34] P. Sainsot, P. Velex, On contact deflection and stiffness in spur and helical gears, Mech. Mach. Theory 154 (2020), https://doi.org/10.1016/j.mechmachtheory.2020.104049.
[35] P. Velex, M. Maatar, A mathematical model for analyzing the influence of shape deviations and mounting errors on gear dynamic behavior, J. Sound Vib. 191 (5) (1996) 629–660, https://doi.org/10.1016/j.jsv.2021.116596.
[36] R.G. Parker, S.M. Vijayakar, T. Imajo, Non-linear dynamic response of a spur gear pair: modelling and experimental comparisons, J. Sound Vib. 237 (3) (2000) 435–455, https://doi.org/10.1006/jsvi.2000.3067.
[37] M. Maatar, P. Velex, Quasi-static and dynamic analysis of narrow-faced helical gears with profile and lead modifications, J. Mech. Des. 119 (4) (1997) 474–480, https://doi.org/10.1115/1.2826392.
[38] P. Velex, A. Saada, Modal analysis for the prediction of dynamic tooth loads in geared trains, in: Proceedings of the 3rd JSME, International. Conference On Motion and Power Transmission, Hiroshima, 1991, pp. 117–122.
[39] P. Velex, M. Ajmi, Dynamic tooth loads and quasi-static transmission errors in helical gears-approximate dynamic factor formulae, Mech. Mach. Theory 42 (11) (2007) 1512–1526, https://doi.org/10.1016/j.mechmachtheory.2006.12.009.
[40] R.M. Lewis, A. Shepherd, V. Torczon, Implementing generating set search methods for linearly constrained minimization, SIAM J. Sci. Comput. 29 (6) (2007) 2507–2530, https://doi.org/10.1137/050635432.
[41] J.J. Stoker, Differential Geometry, John Wiley & Sons, 1969.
[42] K.L. Johnson, Contact Mechanics, Cambridge University Press, 1987.
[43] M. Abramowitz, I.A. Stegun, R.H. Romer, Handbook of Mathematical Functions With formulas, graphs, and Mathematical Tables, 10th ed., National Bureau of Standards, 1972.